An Active Power Support Control Strategy in VSC-HVDC Power Systems Considering Load Characteristics of Electrolytic Aluminum

Xin Ding, Siyang Liao, *Member*, *IEEE*, Jian Xu, *Senior Member*, *IEEE*, and Yuanzhang Sun, *Senior Member*, *IEEE*

***Abstract*—Flexible reserve capacity support is important for mitigating active power imbalance issues in asynchronous power systems. Electrolytic aluminum loads (EALs), owing to their large capacity and rapid response, are used as regulation resources in this study. Combining EALs with renewable energy generation units allows the sending power system to provide active power support to the receiving power system when a large power disturbance occurs. An active power support control strategy is proposed for a voltage source converter based high voltage direct current (VSC-HVDC) asynchronous power system. The active power control method of the EAL is analyzed as the foundation, and the load frequency control models of the sending and receiving systems are presented to promote the proposed control strategy. Active power controllers based on model predictive control (MPC) theory are designed to manage power system uncertainties and external disturbances. The proposed active power support control strategy is realized by optimizing the regulation resources in the sending power system while maintaining a stable frequency when the reserve capacity of the receiving system is insufficient. An actual industrial power grid with renewable energy is selected as the sending system and simulations are performed to verify the effectiveness of the proposed active power support control strategy and MPC-based controllers.**

***Index Terms*—Active power support, asynchronous power system, demand response, electrolytic aluminum load, model predictive control, renewable energy.**

Received: May 20, 2024
Accepted: October 1, 2024
Published Online: May 1, 2025
Xin Ding (corresponding author) is with the School of Electrical Engineering, Shanghai University of Electric Power, Shanghai 200090, China (e-mail: dingxin2016@whu.edu.cn).
Siyang Liao, Jian Xu, and Yuanzhang Sun are with the School of Electrical Engineering and Automation, Wuhan University, Wuhan 430072, China (e-mail: liaosiyang@whu.edu.cn; xujian@whu.edu.cn; yzsun@mail.tsinghua.edu.cn).
DOI:10.23919/PCMP.2023.000293

I. Introduction

The installation of renewable energy in China has progressed rapidly in recent years since the proposal of "carbon peak and carbon neutralization" targets as a major strategic decision in 2020 [1]. However, load centers and renewable energy sources in China are often located thousands of kilometers apart. For instance, the Yunnan province (southwestern region of China) has abundant renewable energy, with hydropower units accounting for 74% of the total installed capacity (79 GW) in 2023 [2]. To further optimize the utilization of the power supply and improve the stability of the overall power system, the China Southern Power Grid (CSG) has promoted voltage source converter based high voltage direct current (VSC-HVDC) asynchronous interconnection projects between the Yunnan power grid and the remainder of the CSG [3]. Owing to their rapid control response in power flow regulation, VSC-HVDC systems can provide additional security support for various emergencies [4].

Maintaining sufficient frequency reserves for HVDC transmission systems is an important research topic. In principle, frequency support regulation methods for asynchronous power systems are primarily related to the control strategies of the converters of the receiving power support (RPS) and sending power support (SPS) systems. For an RPS power system, accurate absorption of unbalanced active power by the VSC-HVDC is key for the RPS converter [5]. Conventional control methods for RPS systems are primarily characterized by: 1) The control reference of the converter is modified using the DC voltage or active-power droop control after introducing an additional signal [6], [7]; and 2) The converter presents the inertia characteristics of synchronous generators using inertia emulation control [8] or virtual synchronous generator (VSG) control [9], [10]. In an SPS power system, the key issue of the SPS converter is to flexibly provide unbalanced active power absorbed by the RPS system. DC voltage droop control methods are primarily applied to SPS converters to realize active power sharing in HVDC systems [11], [12]. Various HVDC controllers have been developed to promote

frequency support based on the general idea of regulating the active power reference setting by introducing a feedback loop. A frequency limit control strategy is proposed on the SPS side of asynchronous interconnection power systems to suppress transient frequency deviation based on practical system testing [13]. Reference [14] designs an adaptive droop controller with a multiterminal HVDC system to improve frequency regulation among asynchronous AC grids, while a frequency droop control strategy that considers a global reference signal is investigated in [15] to provide primary frequency support to an asynchronous HVDC system.

Existing studies regarding frequency support for HVDC asynchronous power systems with renewable energy focus primarily on the design of converter control strategies. However, as the proportion of renewable energy generation increases, the regulation challenges of SPS power systems will become even more severe, e.g., the reserve capacity may be insufficient for managing disturbances [16]. A feasible option for increasing the regulating flexibility of asynchronous power systems is to develop regulation potential on the demand side. As a type of energy-intensive industrial load, electrolytic aluminum enterprises in China are gradually transitioning to southwestern areas with abundant hydropower/wind power (such as the Yunnan province) owing to the electricity price advantage. The rapid response and high capacity of electrolytic aluminum loads (EALs) have been investigated extensively [17], [18], whereas using EALs for smoothing wind power fluctuations has also been investigated [19], [20]. Owing to the asynchronous interconnection between the Yunnan power grid and CSG, the industrial power grid with EALs in the Yunnan power grid, as a type of regulation resources in SPS systems, exhibits significant potential in providing active power support to CSG which has insufficient regulation capacity.

For additional local control strategies, such as droop control and VSG control, the time delay and error caused by the control process may inevitably deteriorate the control performance. However, for asynchronous interconnection power systems with multiple regulation resources, the conventional control strategies cannot effectively manage the system constraints. However, the model predictive control (MPC) method presents significant advantages in addressing external disturbances and system constraint issues, and has been widely used in power system frequency control [21]–[23]. To overcome the disadvantages of droop control, several MPC-based optimization methods have been proposed to promote frequency support and minimize power losses in asynchronous systems [24]– [26]. The control input variables can be further optimized within each sampling period, thereby weakening the error effect.

Considering the insufficient reserve capacity issues in new asynchronous interconnection power systems with a high proportion of renewable energy, this study considers EALs as a type of regulation resource to achieve steady active power support. Owing to its excellent performance in managing system disturbances, the MPC method is adopted in this study to design active power controllers (APCs) to coordinate various regulation resources in SPS and RPS power systems under large power imbalance. The main contributions of this study are summarized as follows.

1) An active power support control architecture for a typical two-terminal VSC-HVDC asynchronous power system is proposed to analyze the frequency control models of sending and receiving power systems.

2) An industrial power grid with multiple regulatory resources is selected as the SPS power system. Combining the regulation potentials of EALs, a coordinated frequency control model of an asynchronous power system is proposed to analyze the active power support controllability while considering the characteristics of the SPS and RPS systems.

3) An MPC-based active power support control strategy is proposed based on the design of APCs for the SPS and RPS systems, which guarantees the maintenance of steady active power support from the SPS system and a stable frequency in the RPS system when a large power imbalance occurs.

The remainder of this paper is organized as follows. Section II introduces the load characteristics and control model of the electrolytic aluminum. The active power support control architecture of the VSC-HVDC asynchronous power system is presented in Section III, along with the frequency control models of the SPS (including hydro generators, wind power, and EALs) and RPS power systems. Section IV introduces the MPC-based active power support control strategy and its design procedure. Simulation results conducted on an actual industrial power grid are presented in Section V. Finally, the conclusions are presented in Section VI.

II. Load Characteristic and Control Model of Electrolytic Aluminum

A. EAL Characteristic

Electrolytic aluminum is generally produced in electrolytic cells via the Hall-Héroult process, where aluminum is decomposed from molten cryolite electrolyte by passing a high direct current (several hundred kiloamperes) into the electrolyzer to generate heat at 950–970 ℃ [27]. As a type of energy-intensive industrial load, EALs have significant regulatory potential owing to their large power capacity (hundreds of megawatts) and high integration. Additionally, the electrolyzer can retain heat for several hours without a power supply, indicating that EALs have heat-storage characteristics for short-term active power regulation.

The electrical and equivalent circuits of an EAL are shown in Fig. 1. In an electrolytic production line, power is supplied from an AC bus and transmitted to the low voltage side of an on-load tap-changer (OLTC) transformer. After passing through the rectification system (including rectification transformers, saturable reactors, and 12 full-bridge rectifiers), a high direct current converges into the DC bus, and the DC voltage U_{DC} drives the electrolysis process. All the electrolytic cells are connected in series, which can be represented by a back electromotive force (EMF) E and resistance R. In general, E and R are constant for each production line. For an actual 330 MW production line, as presented in [28], E and R are equal to 354.6 V and 2.016 mΩ, respectively, based on experimental results.

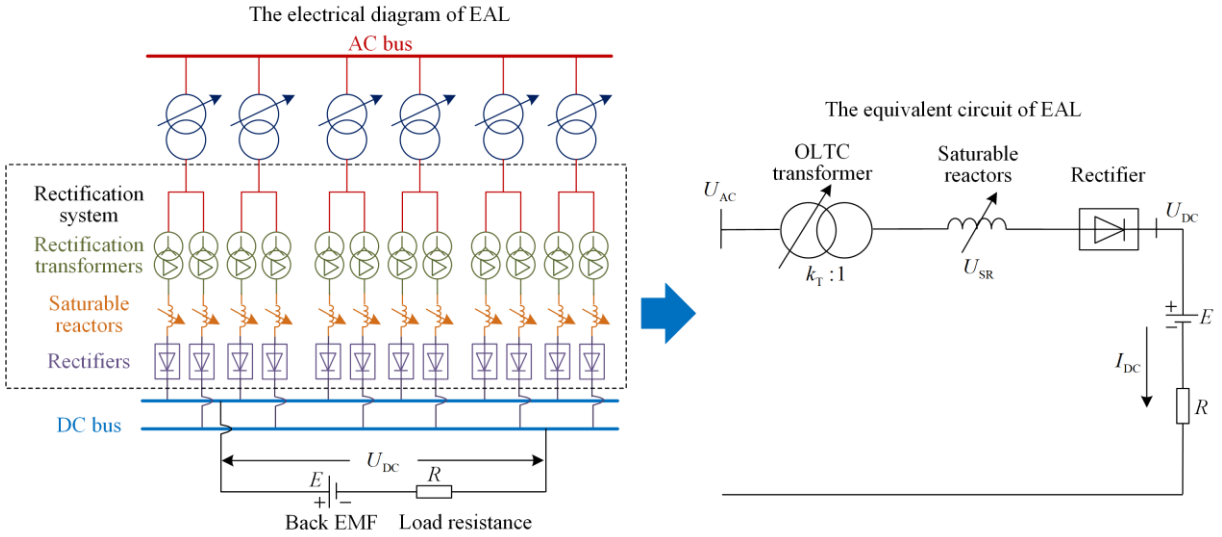

Fig. 1. Electrical diagram and equivalent circuit of EAL.

In Fig. 1, U_{AC} and k_T are the AC bus voltage and the ratio of the OLTC transformer, respectively; U_{SR} is the equivalent voltage drop in the saturable reactors, whose typical values are within 20–40 V and the maximum value allowed is 70 V. The quantitative relation of the voltages between the AC bus U_{AC} and DC bus U_{DC} is given as [17]:

$$U_{DC} = 1.35\left(\frac{U_{AC}}{k_T} - U_{SR}\right) \tag{1}$$

Therefore, the operating direct current in the electrolyzer I_{DC} can be expressed as:

$$I_{DC} = \frac{U_{DC} - E}{R} = \frac{1.35\left(U_{AC}/k_T - U_{SR}\right) - E}{R} \tag{2}$$

The active power consumption of the EAL, P_{EAL}, can be calculated as follows:

$$P_{EAL} = U_{DC} I_{DC} = (I_{DC} R + E) I_{DC} \tag{3}$$

Equation (3) indicates that P_{EAL} is related to the operating direct current I_{DC}. Based on (2), P_{EAL} can be regulated by adjusting the tap changer of the OLTC transformers (i.e., the value of k_T) or by controlling the inductance value L_{SR} of the saturable reactors to change the voltage drop U_{SR} [29]. Compared with the mechanical control on the OLTC transformers, the electronic control on the saturable reactors offers advantages of rapid response (milliseconds class) and continuous regulation, thus rendering it more applicable to the rapid active power regulation in EALs.

B. Control Model of EAL

Combining (1)–(3), once the voltage drops on the saturable reactors are regulated as ΔU_{SR}, the active power deviation of the EAL, ΔP_{EAL}, can be further deduced as follows:

$$\Delta P_{EAL} = R\Delta I_{DC}^2 + R(2I_{DC0} + E)\Delta I_{DC} \tag{4}$$

$$\Delta P_{EAL} = \frac{1.83\Delta U_{SR}^2 + (1.35E - 2.7U_{DC0})\Delta U_{SR}}{R} \tag{5}$$

where I_{DC0} and U_{DC0} are the initial values of direct current; ΔI_{DC} and ΔU_{SR} are the direct current deviation and saturable reactors voltage drops.

Equations (4) and (5) indicate the relationship between ΔP_{EAL} and ΔI_{DC}, ΔU_{SR}, respectively. Taking the actual 330 MW EAL in [28] as an example, I_{DC0} and U_{DC0} are equal to 326.1 kA and 1.012 kV, respectively. Hence, ΔP_{EAL} can be calculated as follows:

$$\begin{cases} \Delta P_{EAL} = 0.002016\Delta I_{DC}^2 + 1315.6\Delta I_{DC} \\ \Delta P_{EAL} = 907\Delta U_{SR}^2 - 1.118\times 10^6 \Delta U_{SR} \end{cases} \tag{6}$$

Owing to the negligible influence from the quadratic terms (ΔI_{DC}^2 and ΔU_{SR}^2), the expressions for ΔP_{EAL} can be simplified to linear forms as follows:

$$\begin{cases} \Delta P_{EAL} \approx R(2I_{DC0} + E)\Delta I_{DC} = K_{P\text{-}I}\Delta I_{DC} \\ \Delta P_{EAL} \approx \dfrac{1.35E - 2.7U_{DC0}}{R}\Delta U_{SR} = K_{P\text{-}U}\Delta U_{SR} \end{cases} \tag{7}$$

where $K_{\text{P-I}}$ and $K_{\text{P-U}}$ are the gain coefficients between ΔP_{EAL} and ΔI_{DC}, ΔU_{SR}, respectively.

Figure 2 illustrates an active power control model of the EAL based on actual production, which includes the transfer functions of the electrolyzer and saturable reactor control circuit. T_{ES} and T_{SR} are the time constants of the electrolyzer and saturable reactor, respectively; K_{i} and K_{p} are the coefficients of the PI controller in the saturable reactor control circuit; I_{DCcon} represents the control current deviation of the saturable reactor; K_{SR} is the control coefficient of the saturable reactor; while ΔU_{SRmax} and ΔU_{SRmin} are the upper and lower limits of the voltage drop ΔU_{SR}, respectively. Thus, the active power of the EAL can be regulated by adjusting the active power reference ΔP_{EALref} The active power response can be written as shown in (8). The active power control model of the EAL can be expressed in the form of differential and state-space equations, as shown in (9) and (10), which serve as the basis for active power support control in the next section.

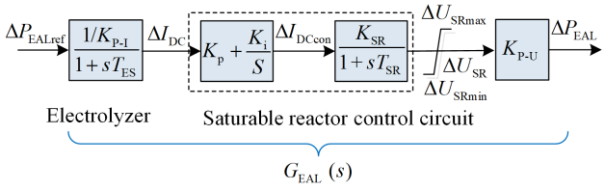

Fig. 2. Active power control model of EAL.

$$G_{\text{EAL}}(s)=\frac{K_{\text{P-U}}K_{\text{SR}}(K_{\text{i}}+sK_{\text{p}})}{K_{\text{P-I}}s(1+sT_{\text{ES}})(1+sT_{\text{SR}})} \tag{8}$$

$$\begin{cases}\Delta\dot{I}_{\text{DC}}=-\dfrac{1}{T_{\text{ES}}}\Delta I_{\text{DC}}+\dfrac{1}{T_{\text{ES}}K_{\text{P-I}}}\Delta P_{\text{EALref}}\\ \Delta\dot{I}_{\text{DCcon}}=\left(K_{\text{i}}-\dfrac{K_{\text{p}}}{T_{\text{ES}}}\right)\Delta I_{\text{DC}}+\dfrac{K_{\text{p}}}{T_{\text{ES}}K_{\text{P-I}}}\Delta P_{\text{EALref}}\\ \Delta\dot{P}_{\text{EAL}}=\dfrac{K_{\text{P-U}}K_{\text{SR}}}{T_{\text{SR}}}\Delta I_{\text{DCcon}}-\dfrac{1}{T_{\text{SR}}}\Delta P_{\text{EAL}}\end{cases} \tag{9}$$

$$\dot{\boldsymbol{x}}_{\text{EAL}}=\boldsymbol{A}_{\text{EAL}}\boldsymbol{x}_{\text{EAL}}+\boldsymbol{B}_{\text{EAL}}\boldsymbol{u}_{\text{EAL}} \tag{10}$$

where $\boldsymbol{x}_{\text{EAL}}$ and $\boldsymbol{u}_{\text{EAL}}$ are the state and control input variables, respectively; meanwhile, $\boldsymbol{A}_{\text{EAL}}$ and $\boldsymbol{B}_{\text{EAL}}$ are the state and control matrices, respectively, expressed as:

$$\begin{cases}\boldsymbol{x}_{\text{EAL}}=\left[\Delta I_{\text{DC}},\Delta I_{\text{DCcon}},\Delta P_{\text{EAL}}\right]^{\text{T}}\\ \boldsymbol{u}_{\text{EAL}}=\Delta P_{\text{EALref}}\\ \boldsymbol{A}_{\text{EAL}}=\begin{bmatrix}-\dfrac{1}{T_{\text{ES}}} & 0 & 0\\ \left(K_{\text{I}}-\dfrac{K_{\text{P}}}{T_{\text{ES}}}\right) & 0 & 0\\ 0 & \dfrac{K_{\text{P-V}}K_{\text{SR}}}{T_{\text{SR}}} & -\dfrac{1}{T_{\text{SR}}}\end{bmatrix}\\ \boldsymbol{B}_{\text{EAL}}=\begin{bmatrix}\dfrac{1}{T_{\text{ES}}K_{\text{P-I}}} & \dfrac{K_{\text{P}}}{T_{\text{ES}}K_{\text{P-I}}} & 0\end{bmatrix}^{\text{T}}\end{cases} \tag{11}$$

The effectiveness of load control on the EAL is presented in Appendix A.

III. Active Power Support Control in Two-Terminal VSC-HVDC Asynchronous Power System

A. Frequency Control Model of SPS and RPS Systems

As mentioned in Section I, owing to the electricity price and policy advantages, electrolytic aluminum production in China is gradually transferred to the Yunnan Province, which has abundant renewable energy sources such as hydropower and wind power. Additionally, the local grid transmits power to the CSG via the VSC-HVDC system and operates in an asynchronous mode. Considering the load characteristics and control model, this paper proposes an active power support control strategy for emergency situations in a typical two-terminal VSC-HVDC asynchronous power system, as shown in Fig. 3.

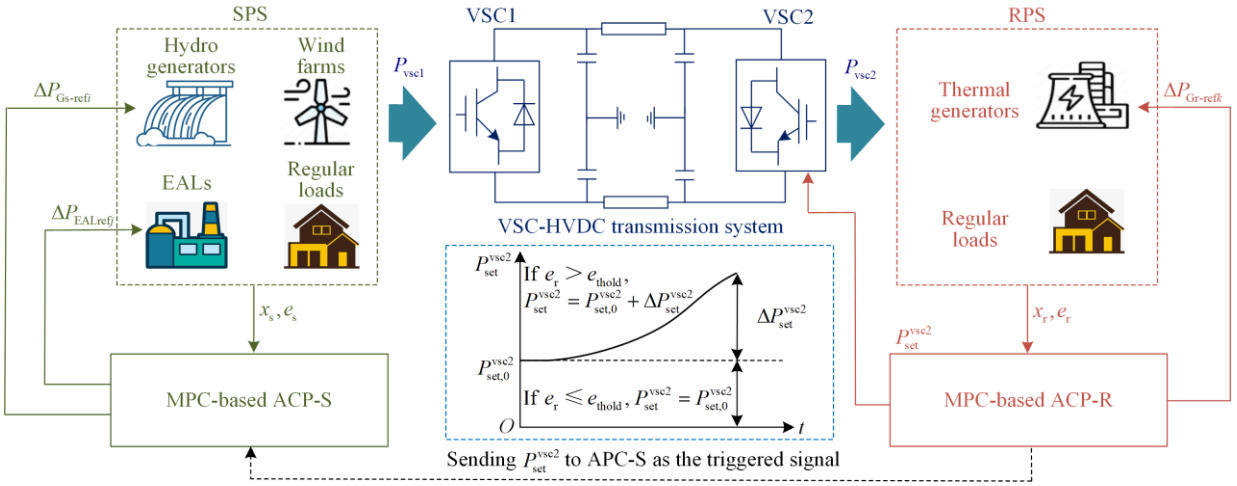

Fig. 3. Active power support control architecture in classical two-terminal VSC-HVDC asynchronous power system.

The active power support control architecture comprises SPS and RPS power systems and a VSC-HVDC transmission system. An industrial regional power system in Yunnan, which includes hydro generators, wind farms, regular loads, and EALs are selected as the SPS system. An RPS comprises the conventional thermal power generators and regular loads. The regulation resources in SPS (hydro generators and EALs) and RPS (thermal generators) systems are controlled by MPC-based APCs. VSC1 and VSC2 are the voltage source converters in the HVDC transmission system. The control process for the active power support control architecture is presented in the next subsection.

The load frequency control (LFC) model of the SPS and RPS systems is shown in Fig. 4, while the notations used in the LFC model are listed in Table I.

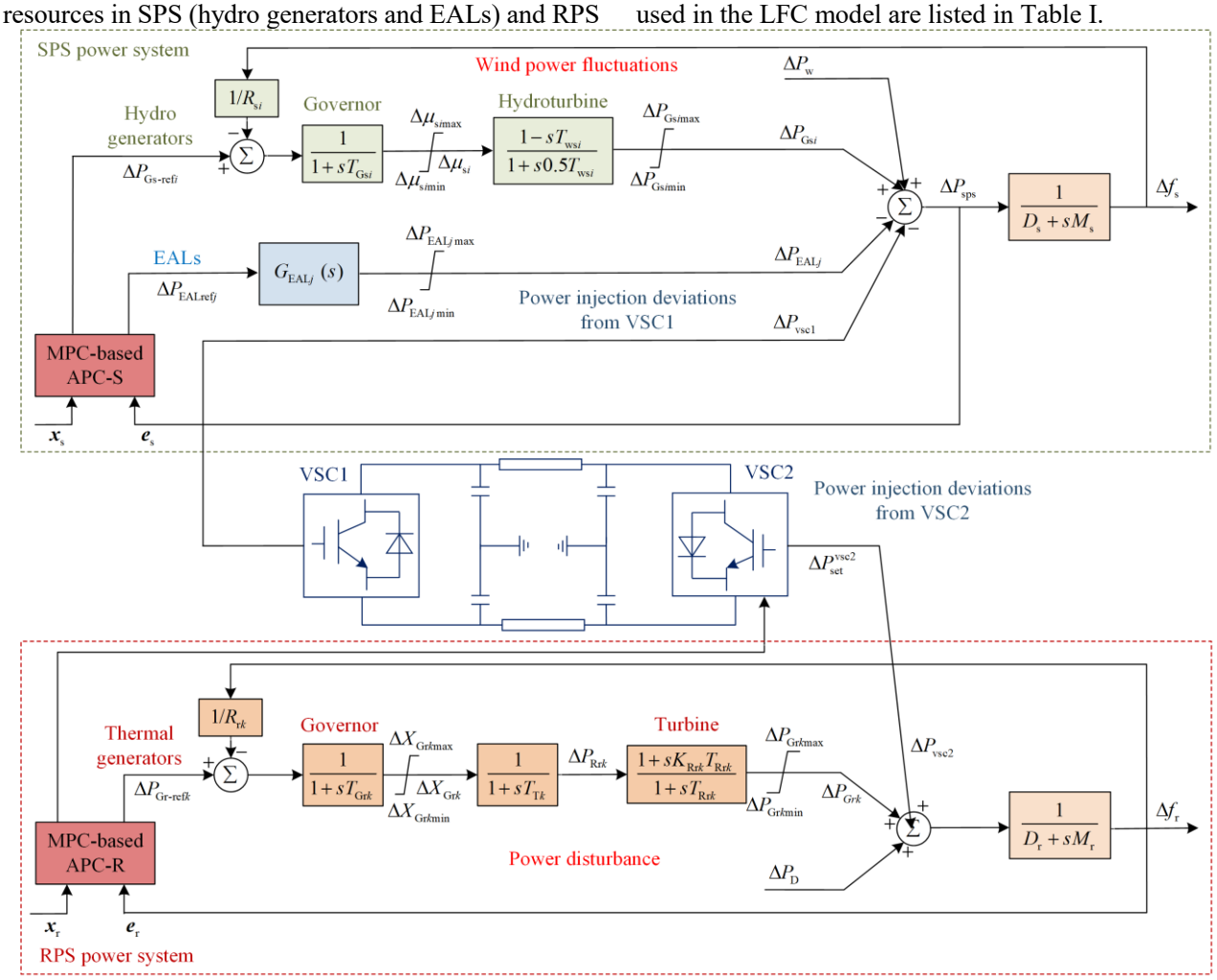

Fig. 4. The LFC model of SPS and RPS power systems.

TABLE I
MEANING OF THE NOTATIONS USED IN LFC MODEL

Notations	Meaning
$1/R_{si}$, $1/R_{tk}$	Frequency-response coefficients of hydro and thermal generators
M_s , M_r	Inertia coefficients of SPS and RPS systems
D_s , D_r	Damp coefficients of SPS and RPS systems
T_{Gsi} , T_{Grk}	Time constants of hydro and thermal governors
$\Delta\mu_{si}$	Guide vane opening of hydro generators
T_{wsi}	Flow time constant of hydro generators
ΔX_{Grk}	Valve-position deviation of thermal governor
T_{Tk} , T_{Rtk}	Time constants of steam turbine and reheater
K_{Rtk}	Fraction of power generated by high-pressure unit
Δf_s , Δf_r	Frequency deviations of SPS and RPS systems

Based on the LFC model, the active power balance equations in the SPS and RPS systems can be expressed as follows:

$$\Delta P_{\text{sps}} = \left(\sum_{i=1}^{m} \Delta P_{\text{G}si} - \sum_{j=1}^{n} \Delta P_{\text{EAL}j} + \Delta P_{\text{w}} \right) - \Delta P_{\text{vsc1}} \tag{12}$$

$$\Delta P_{\text{rps}} = \sum_{k=1}^{l} \Delta P_{\text{G}rk} + \Delta P_{\text{vsc2}} - \Delta P_{\text{D}} \tag{13}$$

where ΔP_{sps} and ΔP_{rps} are the power deviations in the SPS and RPS systems, respectively; $\Delta P_{\text{G}si}/\Delta P_{\text{G}rk}$ and $\Delta P_{\text{EAL}j}$ are the power deviations of hydro/thermal generators and aluminum loads; ΔP_{w} is the wind power fluctuation in the SPS system; ΔP_{D} is the power disturbance in the RPS system; ΔP_{vsc1} and ΔP_{vsc2} are the in-

jection power changes of VSC1 and VSC2, respectively, which can be regulated by adjusting the power transmission value of VSC2, $P_{\text{set}}^{\text{vsc2}}$.

When a power disturbance ΔP_{D} occurs in an RPS system, the active power support control strategy aims to recover the frequency to the nominal value. Owing to the sufficient regulation resources (hydro generators and EALs) in the SPS system, the active power support can be transmitted to the HVDC system by optimizing the power deviations ΔP_{sps} and ΔP_{rps}. Considering the wind power fluctuations ΔP_{w} in the SPS system, a steady active power support should be maintained.

Thus, the active power and frequency deviations are selected as the area control error (ACE) signals in the respective SPS and RPS systems, written as:

$$\begin{cases} e_{\text{s}} = \Delta P_{\text{sps}} \\ e_{\text{r}} = \Delta f_{\text{r}} \end{cases} \tag{14}$$

Based on the LFC models shown in Fig. 4, the frequency control model of the SPS and RPS systems can be expressed as follows (the derivation process is presented in Appendix B):

$$\begin{cases} \dot{\boldsymbol{x}}_{\text{s}} = \boldsymbol{A}_{\text{s}}\boldsymbol{x}_{\text{s}} + \boldsymbol{B}_{\text{s}}\boldsymbol{u}_{\text{s}} + \boldsymbol{P}_{\text{s}}\boldsymbol{d}_{\text{s}} \\ \boldsymbol{y}_{\text{s}} = \boldsymbol{C}_{\text{s}}\boldsymbol{x}_{\text{s}} + \boldsymbol{H}_{\text{s}}\boldsymbol{d}_{\text{s}} \end{cases} \tag{15}$$

$$\begin{cases} \dot{\boldsymbol{x}}_{\text{r}} = \boldsymbol{A}_{\text{r}}\boldsymbol{x}_{\text{r}} + \boldsymbol{B}_{\text{r}}\boldsymbol{u}_{\text{r}} + \boldsymbol{P}_{\text{r}}\boldsymbol{d}_{\text{r}} \\ \boldsymbol{y}_{\text{r}} = \boldsymbol{C}_{\text{r}}\boldsymbol{x}_{\text{r}} \end{cases} \tag{16}$$

where $\boldsymbol{x}_{\text{s}}$ and $\boldsymbol{x}_{\text{r}}$ are the state variables; $\boldsymbol{u}_{\text{s}}$ and $\boldsymbol{u}_{\text{r}}$ are the control inputs; while $\boldsymbol{y}_{\text{s}}$ and $\boldsymbol{y}_{\text{r}}$ are the outputs; meanwhile, $\boldsymbol{d}_{\text{s}}$ and $\boldsymbol{d}_{\text{r}}$ are the disturbances of the SPS and RPS power systems, respectively, expressed as:

$$\begin{cases} \boldsymbol{x}_{\text{s}} = \left[\Delta f_{\text{s}}, \Delta \boldsymbol{P}_{\text{Gs}i}, \Delta \boldsymbol{\mu}_i, \Delta \boldsymbol{I}_{\text{DC}j}, \Delta \boldsymbol{I}_{\text{DCconj}}, \Delta \boldsymbol{P}_{\text{EAL}j}\right]^{\text{T}} \in \boldsymbol{R}^{(1+2i+3j)\times 1} \\ \boldsymbol{u}_{\text{s}} = \left[\Delta \boldsymbol{P}_{\text{Gs-ref}i}, \Delta \boldsymbol{P}_{\text{EALref}j}\right]^{\text{T}} \in \boldsymbol{R}^{(i+j)\times 1} \\ \boldsymbol{y}_{\text{s}} = e_{\text{s}} = \Delta P_{\text{sps}} \\ \boldsymbol{d}_{\text{s}} = \Delta P_{\text{w}} - \Delta P_{\text{vsc1}} \\ \boldsymbol{x}_{\text{r}} = \left[\Delta f_{\text{r}}, \Delta \boldsymbol{P}_{\text{Gr}k}, \Delta \boldsymbol{P}_{\text{R}rk}, \Delta \boldsymbol{X}_{\text{Gr}k}\right]^{\text{T}} \in \boldsymbol{R}^{(1+3k)\times 1} \\ \boldsymbol{u}_{\text{r}} = \left[\Delta \boldsymbol{P}_{\text{Gr-ref}k}, \Delta P_{\text{vsc2}}\right]^{\text{T}} \in \boldsymbol{R}^{(k+1)\times 1} \\ \boldsymbol{y}_{\text{r}} = \Delta f_{\text{r}} \\ \boldsymbol{d}_{\text{r}} = -\Delta P_{\text{D}} \end{cases} \tag{17}$$

The expressions of matrices $\boldsymbol{A}_{\text{s}}$, $\boldsymbol{A}_{\text{r}}$, $\boldsymbol{B}_{\text{s}}$, $\boldsymbol{B}_{\text{r}}$, $\boldsymbol{C}_{\text{s}}$, $\boldsymbol{C}_{\text{r}}$, $\boldsymbol{P}_{\text{s}}$, $\boldsymbol{P}_{\text{r}}$, and $\boldsymbol{H}_{\text{s}}$ in control models (15) and (16) are presented in Appendix B.

B. Active Power Support Control Process

To achieve active power support control, the APCs based on the MPC method are adopted in the SPS and RPS systems to coordinate the regulation resources on the generation and demand sides, as shown in Figs. 3 and 4. The control process of the active power control architecture is presented below.

1) Obtain State Variables and ACE Signals

Using the wide-area measurement system (WAMS) [30], the state variables $\boldsymbol{x}_{\text{s}}$, $\boldsymbol{x}_{\text{r}}$ and the ACE signals e_{s}, e_{r} in the SPS and RPS systems are obtained by the MPC-based APCs. Remote variables and signals can be measured using phasor measurement units and then delivered to MPC-based APCs via rapid communication channels.

2) Implement Control Strategy

The control objective of the APCs is to minimize the ACE signals. To determine the severity of the disturbances in the RPS system, the threshold of the ACE signal e_{thold} is first defined to decide whether to activate the active power control strategy. When an active power disturbance ΔP_{D} occurs in the RPS system, the obtained ACE signal e_{r} is compared with the threshold e_{thold}.

1) When e_{r} is within the threshold e_{thold}, the transmission value of the VSC-HVDC system $P_{\text{set}}^{\text{vsc2}}$ is maintained at the initial value $P_{\text{set,0}}^{\text{vsc2}}$, which implies that $P_{\text{set}}^{\text{vsc2}}$ equals $P_{\text{set,0}}^{\text{vsc2}}$. Thus, the proposed active power support control strategy is not triggered. Instead, a conventional control strategy, such as automatic generation control, is applied in the RPS system to balance the power disturbances.

2) Conversely, when e_{r} is higher than e_{thold}, the APC in the RPS power system (APC-R) computes the power regulation value $\Delta P_{\text{set}}^{\text{vsc2}}$ for VSC2. Consequently, VSC2 regulates its power transmission value $P_{\text{set}}^{\text{vsc2}}$ ($P_{\text{set}}^{\text{vsc2}} = P_{\text{set,0}}^{\text{vsc2}} + \Delta P_{\text{set}}^{\text{vsc2}}$) and transmits it to the APC in the SPS power system (APC-S) as the feedforward signal of the implemented power support control strategy.

3) Optimize Regulation Resources

After implementing the control strategy, the MPC-based APCs optimize the control input variables, such as $\Delta P_{\text{Gs-ref}i}$, $\Delta P_{\text{EALref}j}$, and $\Delta P_{\text{Gr-ref}k}$ (assuming m hydro generators, n EALs, and l thermal generators). The detailed design process of the MPC controllers in the SPS and RPS systems is presented in Section IV. The control input variables are specified to the control units of the regulation resources (hydro generators, EALs, and thermal generators) via the WAMS control station and the network control units (NCUs). Thus, the power deviations in the respective SPS and RPS systems, i.e., ΔP_{sps} and ΔP_{rps}, are regulated to realize the active power support based on (12) and (13). When the ACE signal e_{r} is lower than the required value e_{req}, the active power support control strategy is completed.

The flowchart of the proposed active power support control strategy is shown in Fig. 5.

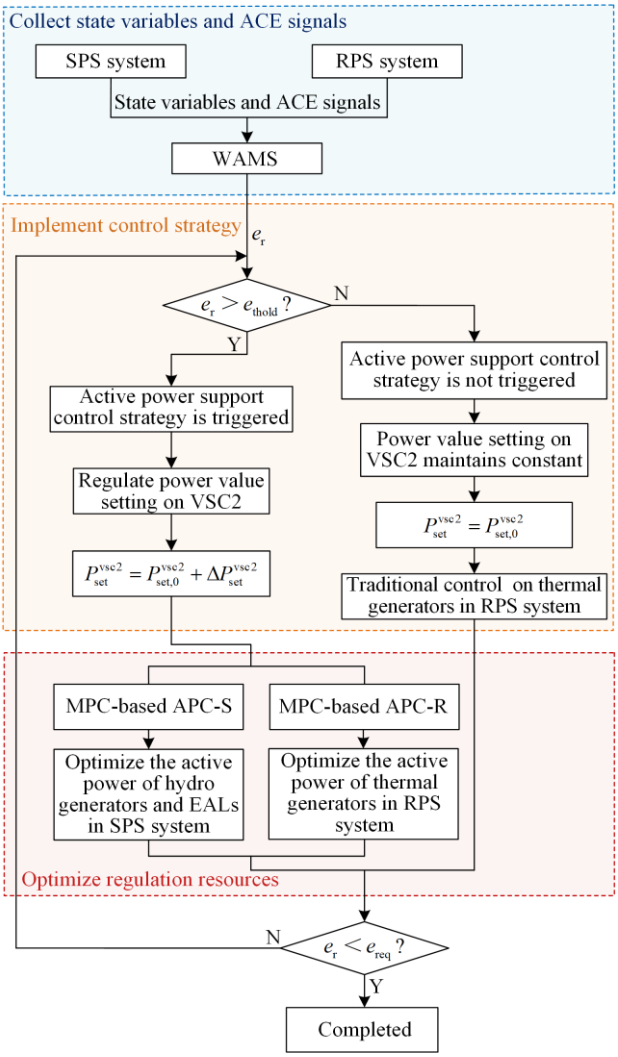

Fig. 5. Flowchart of active power support control strategy.

IV. MPC-BASED ACTIVE POWER SUPPORT CONTROL STRATEGY FOR ASYNCHRONOUS POWER SYSTEMS

As mentioned in Section III, the purpose of the active power support control strategy is to adjust the transmission power in the VSC-HVDC system and coordinate the regulation resources (generation and demand sides) in the asynchronous power systems when a large active power imbalance occurs. Because time-varying wind power fluctuates, the active power support from the SPS system is assumed to be stable. In this case, the proposed active power support control strategy is realized by designing APCs in the SPS and RPS power systems based on the MPC method presented in [22].

A. MPC-based APCs in SPS and RPS Systems

The proposed controllers are designed for large active power disturbance scenarios occurring in RPS systems. Thus, the MPC-based APC-R is first analyzed. Because the MPC method is applied to a discrete system, the frequency control model of the RPS in (16) must be discretized as follows:

$$\begin{cases} \dot{\boldsymbol{x}}_r(K_r+1) = \boldsymbol{A}_{rd}\boldsymbol{x}_r(K_r) + \boldsymbol{B}_{rd}\boldsymbol{u}_r(K_r) + \boldsymbol{P}_{rd}\boldsymbol{d}_r(K_r) \\ \boldsymbol{y}_r(K_r+1) = \boldsymbol{C}_{rd}\boldsymbol{x}_r(K_r) \end{cases} \tag{18}$$

where matrices $\boldsymbol{A}_{rd}$, $\boldsymbol{B}_{rd}$, $\boldsymbol{C}_{rd}$, and $\boldsymbol{P}_{rd}$ are expressed as:

$$\begin{cases} \boldsymbol{A}_{rd} = \mathrm{e}^{\boldsymbol{A}_r T_{s\text{-}r}} \\ \boldsymbol{B}_{rd} = \int_0^{T_{s\text{-}r}} \mathrm{e}^{\boldsymbol{A}_r T_{s\text{-}r}} \mathrm{d}t \boldsymbol{B}_r \\ \boldsymbol{C}_{rd} = \boldsymbol{C}_r \\ \boldsymbol{P}_{rd} = \int_0^{T_{s\text{-}r}} \mathrm{e}^{\boldsymbol{A}_r T_{s\text{-}r}} \mathrm{d}t \boldsymbol{P}_r \end{cases} \tag{19}$$

where $T_{s\text{-}r}$ is the sampling period in the RPS system.

The control objective of the APC-R is to eliminate the ACE signal in the RPS system e_r (e.g., recover the frequency to the normal range) by optimizing the thermal-generator output $\Delta P_{Gr\text{-}ref\!k}$ and injection power change on VSC2, ΔP_{vsc2}. Considering the limits and rate of the generator output and VSC regulation, the receding-horizon optimization model of the APC-R in the RPS system is expressed as follows:

$$\begin{aligned} \min_{\boldsymbol{U}_r(K_r)} J_r\left(\boldsymbol{U}_r(K_r), \boldsymbol{x}_r(K_r)\right) = & \sum_{i_r=0}^{N_{pr}} \left[\boldsymbol{y}_r(K_r+i_r)\right]^{\mathrm{T}} \boldsymbol{Q}_r \boldsymbol{y}_r(K_r+i_r) + \\ & \sum_{i_r=0}^{N_{ur}-1} \left[\boldsymbol{u}_r(K_r+i_r)\right]^{\mathrm{T}} \boldsymbol{R}_r \boldsymbol{u}_r(K_r+i_r), \end{aligned}$$

$$\text{s.t.} \begin{cases} \boldsymbol{x}_r(K_r+i_r+1\,|\,K_r) = \boldsymbol{A}_{rd}\boldsymbol{x}_r(K_r+i_r\,|\,K_r) + \\ \boldsymbol{B}_{rd}\boldsymbol{u}_r(K_r+i_r\,|\,K_r) + \boldsymbol{P}_{rd}\boldsymbol{d}_r(K_r+i_r\,|\,K_r), i_r \geqslant 0 \\ \boldsymbol{x}_r(K_r\,|\,K_r) = \boldsymbol{x}_{rK_r} \\ \boldsymbol{d}_r(K_r\,|\,K_r) = \boldsymbol{d}_{rK_r} \\ \boldsymbol{y}_r(K_r+i_r\,|\,K_r) = \boldsymbol{C}_{rd}\boldsymbol{x}_r(K_r+i_r\,|\,K_r), i_r \geqslant 0 \\ \boldsymbol{x}_{r\min} \leqslant \boldsymbol{x}_r(K_r+i_r\,|\,K_r) \leqslant \boldsymbol{x}_{r\max}, i_r = 0,\cdots, N_{pr}-1 \\ \Delta\boldsymbol{x}_{r\min} \leqslant \Delta\boldsymbol{x}_r(K_r+i_r\,|\,K_r) \leqslant \Delta\boldsymbol{x}_{r\max}, i_r = 0,\cdots, N_{pr}-1 \\ \boldsymbol{u}_{r\min} \leqslant \boldsymbol{u}_r(K_r+i_r\,|\,K_r) \leqslant \boldsymbol{u}_{r\max}, i_r = 0,\cdots, N_{ur}-1 \\ \Delta\boldsymbol{u}_{r\min} \leqslant \Delta\boldsymbol{u}_r(K_r+i_r\,|\,K_r) \leqslant \Delta\boldsymbol{u}_{r\max}, i_r = 0,\cdots, N_{ur}-1 \end{cases} \tag{20}$$

where N_{pr} and N_{ur} are the predictive and control time domains, respectively; $\boldsymbol{U}_r(K_r)$ is the optimal control sequence at time K_r, which is defined as $\boldsymbol{U}_r(K_r) = \left[\boldsymbol{u}_r(K_r),\cdots,\boldsymbol{u}_r(K_r+N_{ur}-1)\right]^{\mathrm{T}}$; $\boldsymbol{Q}_r$ and $\boldsymbol{R}_r$ are the weight coefficient matrices for the cost function $J_r(\boldsymbol{U}_r(K_r), \boldsymbol{x}_r(K_r))$; $\boldsymbol{x}_r(K_r+i_r\,|\,K_r)$ and $\boldsymbol{u}_r(K_r+i_r\,|\,K_r)$ are the predictive state and control input within N_{pr} and N_{ur} at time (K_r+i_r), respectively.

During each control step, the APC-R obtains the state $\boldsymbol{x}_r(K_r)$ and computes the optimal control sequence $\boldsymbol{u}_r(K_r)$ by solving the quadratic programming problem in the optimization model in (14). The first optimal solution $\boldsymbol{u}_r(K_r)$ in the optimal control sequence $\boldsymbol{U}_r(K_r)$ is selected as the control input for the discretized control model in (18). Thus, the optimal values of $\Delta P_{Gr\text{-}ref\!k}$ and ΔP_{vsc2} in each step can be obtained.

The transmission power regulation in the HVDC system P_{set}^{vsc2} is adjusted based on the optimal value of

ΔP_{vsc2}. The updated $P_{\text{set}}^{\text{vsc2}}$ is transmitted to the MPC-based APC-S in the SPS power system as a triggered signal. Thus, the regulation resources in the SPS system, including the active power of the hydro generators and EALs, can be optimized using the APC-S.

Similarly, the control strategy in the APC-S is realized using the MPC method. First, the frequency control model of the SPS system expressed in (15) is discretized as follows:

$$\begin{cases} \dot{\boldsymbol{x}}_{\text{s}}(K_{\text{s}}+1) = \boldsymbol{A}_{\text{sd}}\boldsymbol{x}_{\text{s}}(K_{\text{s}}) + \boldsymbol{B}_{\text{sd}}\boldsymbol{u}_{\text{s}}(K_{\text{s}}) + \boldsymbol{P}_{\text{sd}}\boldsymbol{d}_{\text{s}}(K_{\text{s}}) \\ \boldsymbol{y}_{\text{s}}(K_{\text{s}}+1) = \boldsymbol{C}_{\text{sd}}\boldsymbol{x}_{\text{s}}(K_{\text{s}}) + \boldsymbol{H}_{\text{sd}}\boldsymbol{d}_{\text{s}}(K_{\text{s}}) \end{cases} \tag{21}$$

where the discretized matrices $\boldsymbol{A}_{\text{sd}}$, $\boldsymbol{B}_{\text{sd}}$, $\boldsymbol{C}_{\text{sd}}$, $\boldsymbol{P}_{\text{sd}}$, and $\boldsymbol{H}_{\text{sd}}$ are expressed as follows:

$$\begin{cases} \boldsymbol{A}_{\text{sd}} = \text{e}^{\boldsymbol{A}_{\text{s}}T_{\text{s-s}}} \\ \boldsymbol{B}_{\text{sd}} = \int_0^{T_{\text{s-s}}} \text{e}^{\boldsymbol{A}_{\text{s}}T_{\text{s-s}}}\text{d}t\boldsymbol{B}_{\text{s}} \\ \boldsymbol{C}_{\text{sd}} = \boldsymbol{C}_{\text{s}} \\ \boldsymbol{P}_{\text{sd}} = \int_0^{T_{\text{s-s}}} \text{e}^{\boldsymbol{A}_{\text{s}}T_{\text{s-s}}}\text{d}t\boldsymbol{P}_{\text{s}} \\ \boldsymbol{H}_{\text{sd}} = \boldsymbol{H}_{\text{s}} \end{cases} \tag{22}$$

where $T_{\text{s-s}}$ is the sampling period in the SPS system.

The aim of the APC-S is to regulate the hydro generator output $\Delta P_{\text{Gs-ref}i}$ and the EAs power reference $\Delta P_{\text{EALref}j}$, thus providing active power support to VSC1, ΔP_{vsc1}, and enabling the monitoring of the injection power change on VSC2, i.e., ΔP_{vsc2}. Additionally, considering the time-varying wind power fluctuations, the ACE signal in the SPS system e_{s} (e.g., the active power deviation in the SPS, ΔP_{sps}) should be eliminated.

Thus, combining (12), (14), and (15), the receding-horizon optimization model of the APC-S in the SPS system is expressed as follows:

$$\begin{aligned} \min_{\boldsymbol{U}_{\text{s}}(K_{\text{s}})} J_{\text{s}}(\boldsymbol{U}_{\text{s}}(K_{\text{s}}), \boldsymbol{x}_{\text{s}}(K_{\text{s}})) = & \sum_{i_{\text{s}}=0}^{N_{\text{ps}}} \left[\boldsymbol{y}_{\text{s}}(K_{\text{s}}+i_{\text{s}})\right]^{\text{T}} \boldsymbol{Q}_{\text{s}} \boldsymbol{y}_{\text{s}}(K_{\text{s}}+i_{\text{s}}) + \\ & \sum_{i_{\text{s}}=0}^{N_{\text{us}}-1} \left[\boldsymbol{u}_{\text{s}}(K_{\text{s}}+i_{\text{s}})\right]^{\text{T}} \boldsymbol{R}_{\text{s}} \boldsymbol{u}_{\text{s}}(K_{\text{s}}+i_{\text{s}}), \end{aligned}$$

$$\text{s.t.} \begin{cases} \boldsymbol{x}_{\text{s}}(K_{\text{s}}+i_{\text{s}}+1 \mid K_{\text{s}}) = \boldsymbol{A}_{\text{sd}}\boldsymbol{x}_{\text{s}}(K_{\text{s}}+i_{\text{s}} \mid K_{\text{s}}) + \\ \boldsymbol{B}_{\text{sd}}\boldsymbol{u}_{\text{s}}(K_{\text{s}}+i_{\text{s}} \mid K_{\text{s}}) + \boldsymbol{P}_{\text{sd}}\boldsymbol{d}_{\text{s}}(K_{\text{s}}+i_{\text{s}} \mid K_{\text{s}}), i_{\text{s}} \geqslant 0 \\ \boldsymbol{x}_{\text{s}}(K_{\text{s}} \mid K_{\text{s}}) = \boldsymbol{x}_{\text{s}K_{\text{s}}} \\ \boldsymbol{d}_{\text{s}}(K_{\text{s}} \mid K_{\text{s}}) = \boldsymbol{d}_{\text{s}K_{\text{s}}} \\ \boldsymbol{y}_{\text{s}}(K_{\text{s}}+i_{\text{s}} \mid K_{\text{s}}) = \boldsymbol{C}_{\text{sd}}\boldsymbol{x}_{\text{s}}(K_{\text{s}}+i_{\text{s}} \mid K_{\text{s}}) + \\ \qquad \boldsymbol{H}_{\text{sd}}\boldsymbol{d}_{\text{s}}(K_{\text{s}}+i_{\text{s}} \mid K_{\text{s}}), i_{\text{s}} \geqslant 0 \\ \boldsymbol{x}_{\text{s}\min} \leqslant \boldsymbol{x}_{\text{s}}(K_{\text{s}}+i_{\text{s}} \mid K_{\text{s}}) \leqslant \boldsymbol{x}_{\text{s}\max}, i_{\text{s}} = 0, \cdots, N_{\text{ps}}-1 \\ \Delta\boldsymbol{x}_{\text{s}\min} \leqslant \Delta\boldsymbol{x}_{\text{s}}(K_{\text{s}}+i_{\text{s}} \mid K_{\text{s}}) \leqslant \Delta\boldsymbol{x}_{\text{s}\max}, i_{\text{s}} = 0, \cdots, N_{\text{ps}}-1 \\ \boldsymbol{u}_{\text{s}\min} \leqslant \boldsymbol{u}_{\text{s}}(K_{\text{s}}+i_{\text{s}} \mid K_{\text{s}}) \leqslant \boldsymbol{u}_{\text{s}\max}, i_{\text{s}} = 0, \cdots, N_{\text{us}}-1 \\ \Delta\boldsymbol{u}_{\text{s}\min} \leqslant \Delta\boldsymbol{u}_{\text{s}}(K_{\text{s}}+i_{\text{s}} \mid K_{\text{s}}) \leqslant \Delta\boldsymbol{u}_{\text{s}\max}, i_{\text{s}} = 0, \cdots, N_{\text{us}}-1 \end{cases} \tag{23}$$

where the nomenclatures used in the receding-horizon optimization model (23) are similar to those used in model (20); N_{ps} and N_{us} are the predictive and control time domains, respectively; $\boldsymbol{Q}_{\text{s}}$ and $\boldsymbol{R}_{\text{s}}$ represent the weight coefficient matrices for the cost function; and $J_{\text{s}}(\boldsymbol{U}_{\text{s}}(K_{\text{s}}), \boldsymbol{x}_{\text{s}}(K_{\text{s}}))$ is the control input of the APC-S, which is determined by the first optimal solution $\boldsymbol{u}_{\text{s}}(K_{\text{s}})$ in $\boldsymbol{U}_{\text{s}}(K_{\text{s}})$ (the optimal control sequence at time K_{s}) after solving the optimization problem in (23).

The control performance of the MPC method is affected by matrices $\boldsymbol{Q}$ and $\boldsymbol{R}$, which represent the error-tracking effect and control input cost, respectively. To achieve more flexible regulation, time-varying weight matrices are applied to the design controllers. In this study, matrices $\boldsymbol{Q}_{\text{r}}$ and $\boldsymbol{Q}_{\text{s}}$ are constant, whereas matrices $\boldsymbol{R}_{\text{r}}$ and $\boldsymbol{R}_{\text{s}}$ vary with the feedback-error deviation, as:

$$\begin{cases} \boldsymbol{R}_{\text{r}} = \boldsymbol{R}_{\text{r0}} - \boldsymbol{W}_{\text{r}}e_{\text{r}} = \boldsymbol{R}_{\text{r0}} - \boldsymbol{W}_{\text{r}}\Delta f_{\text{r}} \\ \boldsymbol{R}_{\text{s}} = \boldsymbol{R}_{\text{s0}} - \boldsymbol{W}_{\text{s}}e_{\text{s}} = \boldsymbol{R}_{\text{s0}} - \boldsymbol{W}_{\text{s}}\Delta P_{\text{sps}} \end{cases} \tag{24}$$

where $\boldsymbol{R}_{\text{r0}}$ and $\boldsymbol{R}_{\text{s0}}$ are the initial standard matrices; while $\boldsymbol{W}_{\text{r}}$ and $\boldsymbol{W}_{\text{s}}$ are the droop coefficient matrices for $\boldsymbol{R}_{\text{r}}$ and $\boldsymbol{R}_{\text{s}}$, respectively. The controllers prefer tracking errors to achieve better transient performance if the deviations enlarge. When the errors are small, the controllers tend to achieve better stability against disturbances.

Therefore, the regulation resources in the SPS system, including hydro generators and EALs, can be regulated to provide active power support to the RPS system via the VSC-HVDC transmission system and facilitate the recovery of the frequency to its nominal value, even though wind power fluctuation ΔP_{w} and power disturbance ΔP_{D} exist.

B. Implementation of Active power support Control Strategy

The design procedure for the MPC-based active power support control strategy is as follows.

1) Determine Whether to Activate Control Strategy

As mentioned in Section III, the MPC-based APCs aim to minimize the ACE in the SPS and RPS power systems. When active power disturbance occurs in the RPS power system, its frequency f_{r} deviates from the normal value. Consequently, the frequency-deviation Δf_{r} in the RPS system is measured as the ACE signal e_{r}. Similarly, the active power deviation ΔP_{sps} is selected as the ACE e_{s} in the SPS system based on the LFC model. Subsequently, the obtained ACE signal e_{r} is compared with the threshold e_{thold}. The active power support control strategy is activated if e_{r} is higher than the threshold e_{thold}, and vice versa.

2) Construct MPC-based Controllers

Once the control strategy is activated, the APC in the RPS power system computes the power regulation value $\Delta P_{\text{set}}^{\text{vsc2}}$ on VSC2, which implies that the power transmission value $P_{\text{set}}^{\text{vsc2}}$ on the VSC-HVDC system will be

regulated. Meanwhile, the revised value of $P_{\text{set}}^{\text{vsc2}}$ is sent to the SPS system as a feedforward signal.

The APCs in the SPS and RPS systems obtain the state variables $\boldsymbol{x}_{\text{s}}$ and $\boldsymbol{x}_{\text{r}}$ (the variables in the hydro generators, thermal generators, and EALs are presented in Section III.A). Combining the regulating constraints of the generators and EALs, discretized prediction models in (18) and (21) and optimization models in (20) and (23) in the SPS and RPS power systems are constructed.

3) Solve Receding-horizon Optimization Problems

Once the prediction models are established, during each sampling period, the receding-horizon optimization problems in (20) and (23) are solved after calculating for the linear-quadratic optimal control issues. Subsequently, the first optimal solution in the optimal control sequence is selected as the control input for the receding-horizon optimization problems. Thus, the optimal control inputs $\boldsymbol{u}_{\text{s}}$ and $\boldsymbol{u}_{\text{r}}$ in the SPS and RPS systems for each period are obtained using the MPC-based APCs.

4) Provide Regulation Commands to Control Subjects

After calculating the optimal solution, the ACPs transmit the optimal control inputs, $\boldsymbol{u}_{\text{s}}$ and $\boldsymbol{u}_{\text{r}}$, to the NCUs. Subsequently, regulation commands are provided to the control subjects. In the RPS system, the optimal values of $\Delta P_{\text{Gr-ref}k}$ and ΔP_{vsc2} are transmitted as the control inputs of the thermal generators and VSC2. Meanwhile, in the SPS system, the regulation resources, such as hydro generators and EALs, are adjusted after the optimal values of $\Delta P_{\text{Gs-ref}i}$ and $\Delta P_{\text{EALref}j}$ are received. Thus, the power deviations in the SPS and RPS systems ΔP_{sps} and ΔP_{rps} can be regulated, thereby achieving active power support. Consequently, similar to the ACE in the RPS system, the frequency deviation Δf_{r} can be minimized.

The details on the design procedure for the MPC-based active power support control strategy are shown in Fig. 6. The effectiveness of the proposed control strategy is validated in the following section.

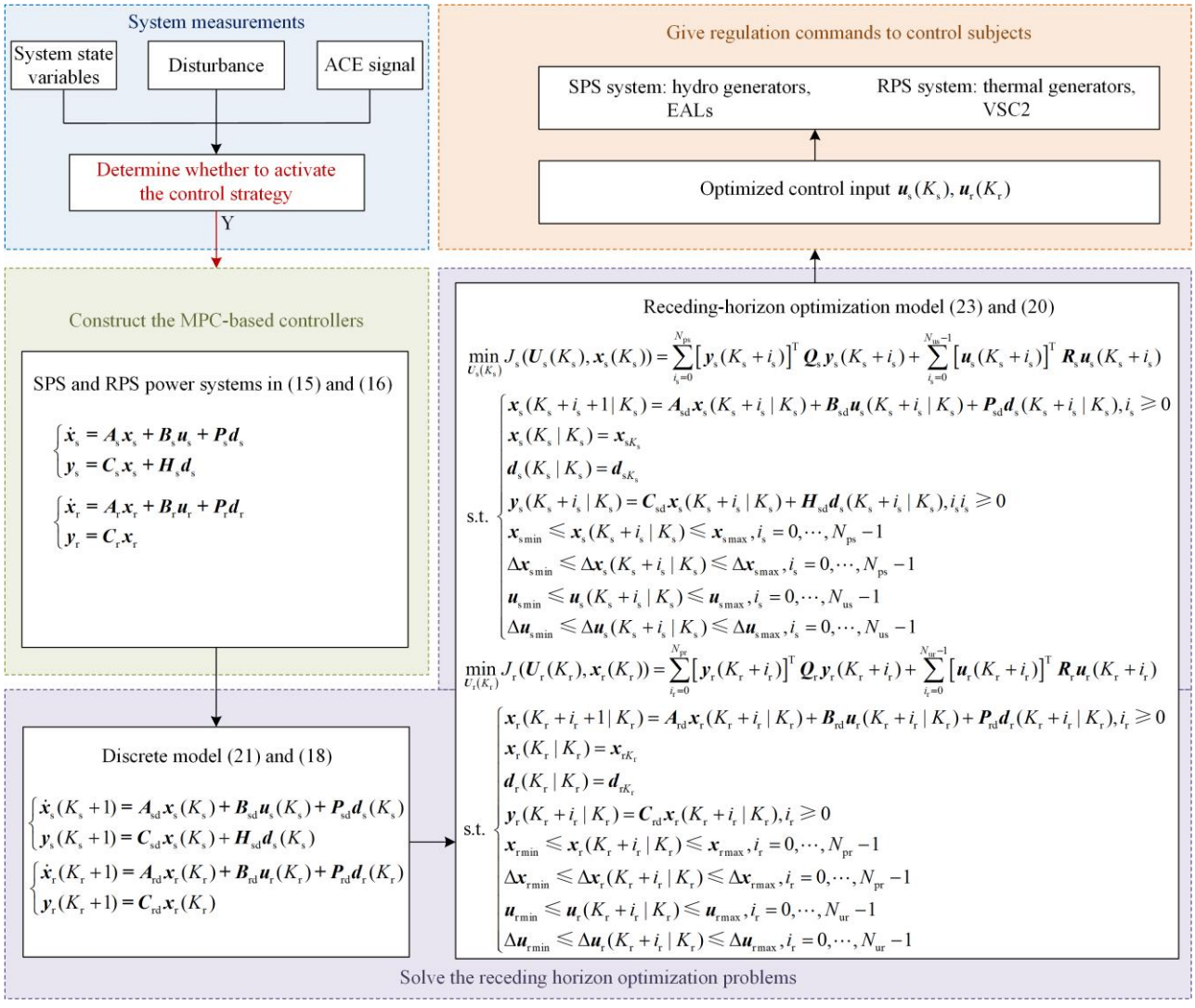

Fig. 6. Diagram of MPC-based active power support control strategy.

V. Simulations and Analysis

A. Small Power Disturbance in RPS System

To verify the performance of the proposed active power support control strategy, an actual power system with a high proportion of hydropower and EAL in the Yunnan power grid is selected as the SPS system and the IEEE 39-bus system is selected as the RPS system, as shown in Fig. 7. The SPS and RPS power systems are connected using VSC-HVDC transmission lines. In the SPS system, G1-G2 are thermal generators and G3–G11 are hydro generators with an installed capacity of 85%. A wind farm is installed at Bus 30 with a period of wind fluctuation, as shown in Fig. 8. VSC1 and VSC2 are connected to Buses S27 and R39, respectively. The VSC-HVDC asynchronous power system mentioned above is tested on an RTDS platform.

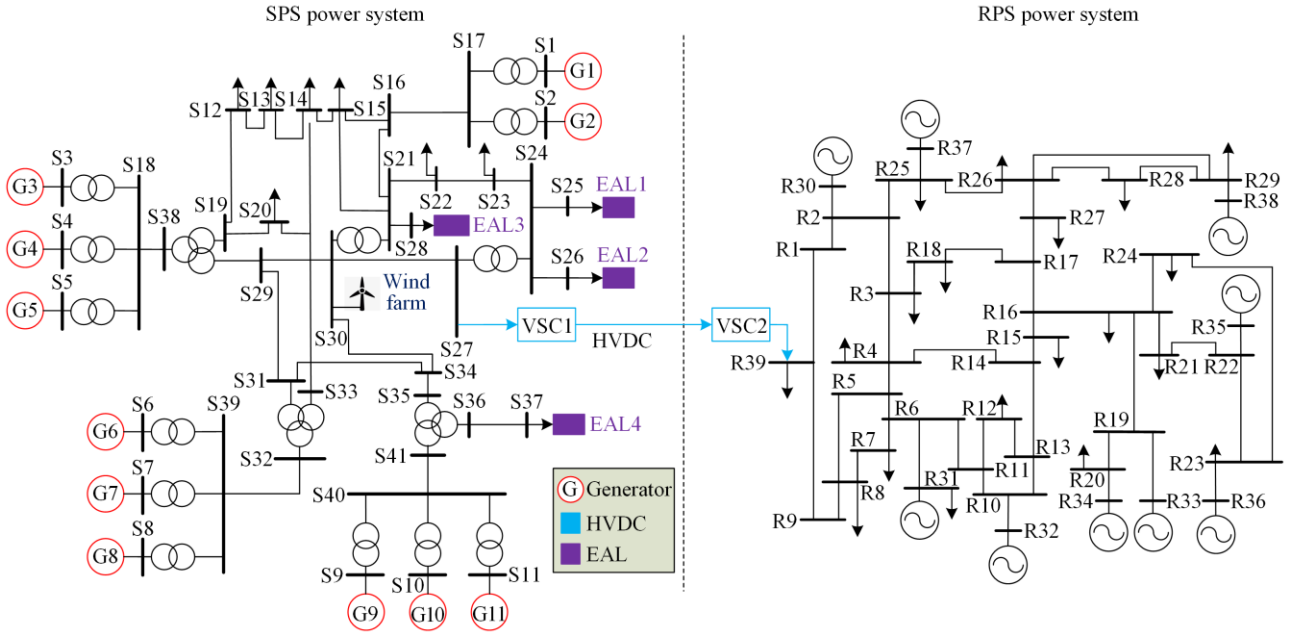

Fig. 7. Structure of VSC-HVDC asynchronous power system.

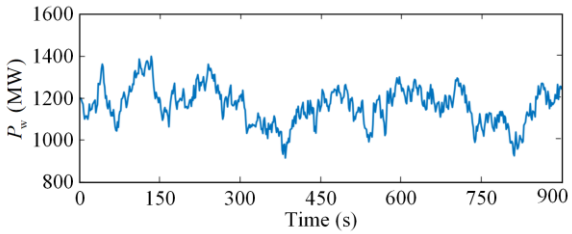

Fig. 8. Power fluctuations of wind farm in SPS power system.

The installed capacities of the generators and the loads of the SPS power system are listed in Table II. The total installed capacity of the loads in the RPS is 6200 MW. The initial transmitted power of the VSC-HVDC system is 1000 MW.

In this case, the active power on load bus R4 in the RPS power system increases abruptly by 200 MW (accounting for approximately 3% of the total capacity on the demand side), thus causing a small power disturbance in the RPS system. Consequently, the frequency in the RPS f_r decreases owing to the power imbalance, as presented in Fig. 9, whereas the ACE signal e_r remains within the threshold e_{thold} (0.2 Hz in this study). Therefore, the active power support control strategy is not activated, and the transmission power of the VSC-HVDC system does not change. Additionally, the small power disturbance is concealed by regulating the MPC-based APC-R, and the thermal generator output $\Delta P_{Gr\text{-}ref k}$ is optimized to recover the frequency deviation Δf_r in the RPS system. Meanwhile, the MPC-based APC-S optimizes the hydro generators output $\Delta P_{Gs\text{-}ref i}$ and EAL power consumption $\Delta P_{EALref j}$ to smooth the wind power fluctuation ΔP_w in the SPS power system, thus resulting in a stable power transmission ΔP_{sps} from the SPS system to the HVDC lines.

TABLE II
Installed Capacity of Generators and Loads in SPS Power System

Generators/loads	Installed capacity (MW)
G1/G2	400
G3/G4	600
G6/G7/G8	500
G9/G10/G11	800
Wind farm	1500
EAL1/EAL2/EAL3/EAL4	800
Regular loads (total)	1300

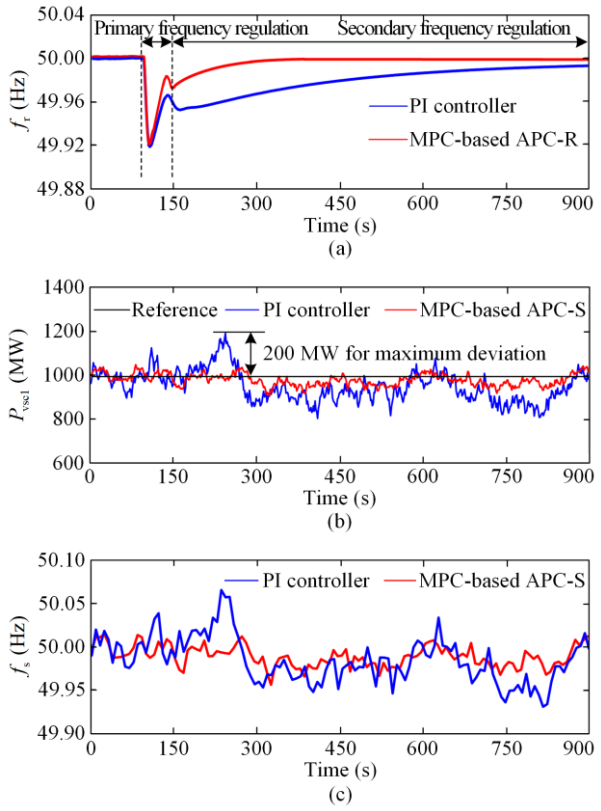

Fig. 9. Control effects of MPC-based controller and PI controller under small power disturbance in RPS power system. (a) Frequency in RPS system f_r. (b) Frequency in SPS system f_s. (c) Injection power of VSC1 in SPS system P_{vsc1}.

In this subsection, the PI control method is selected for comparison. The PI parameters in the SPS and RPS power systems are $K_{Ps}=8.0$, $K_{Is}=1.5$ and $K_{pr}=10.0$, $K_{Ir}=1.5$. A small power disturbance occurs at $t=100$ s with a step increase of 200 MW load power on Bus R4. The frequencies in the RPS and SPS systems and the effects of the two control methods are shown in Fig. 9.

When the small power disturbance occurs, the frequency in the RPS power system f_r decreases to 49.92 Hz and then recovers to the nominal value via the two controllers. Compared with the PI controller, the MPC-based ACP-R performs better in terms of frequency recovery, resulting in shorter recovery times for the primary and secondary frequency regulations. In the SPS power system, the reference output power of the SPS, P_{vsc1}, is 1000 MW, because the active power support control strategy is not activated. The control objectives of the PI controller and MPC-based ACP-S are to smooth the wind power fluctuations (shown in Fig. 7) and maintain a stable injection power for VSC1, P_{vsc1}. The simulation results indicate that the MPC-based ACP-S decreases the power deviation within ±50 MW, whereas the PI controller results in a maximum error of 200 MW. Consequently, the frequency in the SPS system f_s became more stable owing to the MPC-based ACP-S, as shown in Fig. 9(b).

B. Large Power Disturbance in RPS System

For large power disturbance scenarios in the RPS power system, two cases are considered (i.e., active power shortage and surplus in the RPS system) to test the proposed active power support control strategy in asynchronous systems.

During an active power shortage, a thermal generator on Bus R32 is not functioning because of a short-circuit fault at $t=100$ s. This results in a 650 MW power shortage in the RPS system, constituting approximately 10.5% of the total load capacity, and leads to a rapid decrease in the frequency. In the active power surplus case, the power of the load on Bus R8 is decreased abruptly by 600 MW at $t=100$ s, resulting in frequency increase. To ensure that the frequency in the RPS system is recovered to the normal range after the occurrence of the large power disturbances, four different control strategies are applied in two cases for comparison, as listed in Table III.

TABLE III
CONTROL STRATEGIES APPLIED TO SPS AND RPS POWER SYSTEMS FOR TWO CASES

Control Strategy		SPS system	RPS system
A	No active power support	**MPC-based ACP-S**	**MPC-based ACP-R**
B	**With active power support**	PI controller	PI controller
C	**With active power support**	**MPC-based ACP-S**; no regulation on EALs	**MPC-based ACP-R**
D	**With active power support**	**MPC-based ACP-S; with regulation on EALs**	**MPC-based ACP-R**

In contrast to Strategies B, C, and D, the active power support control strategy of asynchronous power systems is not applied to Strategy A. PI controllers are used in Strategy B, whereas the proposed MPC-based controllers are applied to Strategies C and D for comparison. Strategies C and D differ in terms of whether the power consumption of the EALs is regulated.

The control effects of the different strategies are illustrated in Fig. 10. The frequency in the RPS power system f_r is shown in Fig. 10(a), which indicates that the proposed active power support control strategy promotes the recovery of the frequency to nominal values. Additionally, compared with the PI controller (Strategy B), the MPC-based ACPs (Strategies C and D) exhibit better performance with shorter recovery time.

When the active power support control strategy of asynchronous power systems is activated, the MPC-based ACP-R computes the optimal power regulation on VSC2 P_{vsc2}, and changes its power transmis-

sion value $P_{\text{set}}^{\text{vsc2}}$. After the MPC-based ACP-S receives a power transmission value, the output power reference of VSC1, P_{vsc1}, in the SPS system is changed from 1000 to 1300 MW. Owing to the rapid regulation of the EALs, Strategy D performs better than Strategy C in terms of smoothing wind power fluctuations and monitoring the reference, as shown in Fig. 10(b). Based on the receding-horizon optimization of the MPC method, the power consumption of the EAL, P_{EAL}, decreases from 3200 MW to 2900 MW and remained steady once the active power support control strategy is activated, as shown in Fig. 10(c).

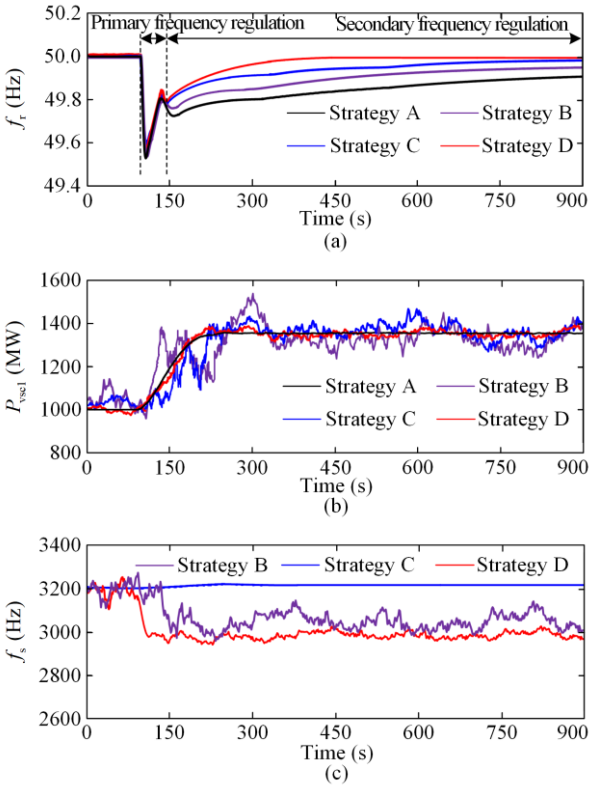

Fig. 10. Control effects of different strategies under active power shortage in RPS system. (a) Frequency in RPS system f_r. (b) Injection power of VSC1 in SPS system P_{vsc1}. (c) Active power consumption of EALs in SPS system P_{EAL}.

The simulation results for the active power surplus case in the RPS are shown are presented in Fig. 11. The frequency in the RPS system f_r increases when a large active power disturbance occurs. Similarly, compared with the PI controller (Strategy B), the MPC-based ACPs (Strategies C and D) exhibit better performance during the secondary frequency regulation. When the active power support control strategy of asynchronous power systems is involved, the MPC-based ACP-R optimize the power regulation on VSC2, and the output power reference of VSC1, P_{vsc1}, in the SPS system decreased from 1000 MW to 640 MW, as shown in Fig. 11(b). Compared with the PI control method, the MPC-based ACP-S can optimize the entire output power of the SPS system to monitor the reference. Owing to the rapid response of the EALs, wind power fluctuations are stabilized, resulting in a smoother output for VSC1 in Strategy D.

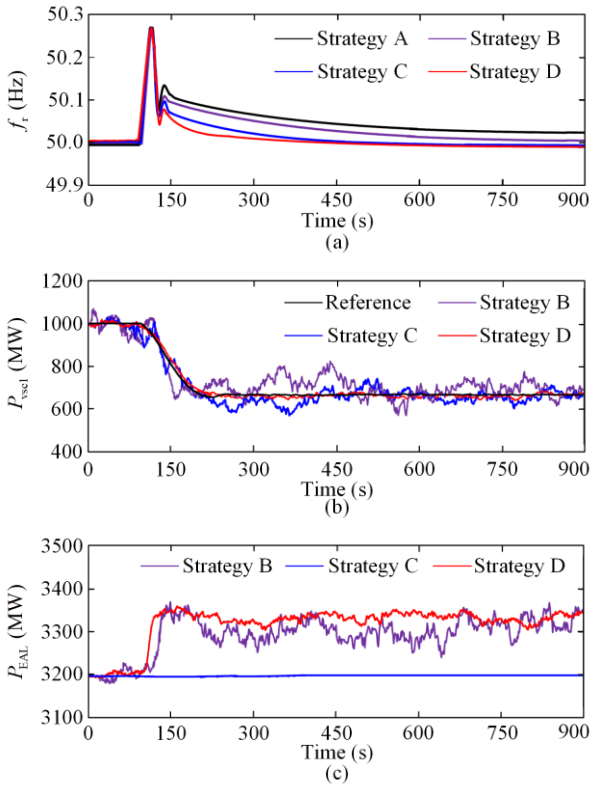

Fig. 11. Control effects of different strategies under active power surplus in RPS system. (a) Frequency in RPS system f_r. (b) Injection power of VSC1 in SPS system P_{vsc1}. (c) Active power consumption of EALs in SPS system P_{EAL}.

C. Robustness Discussion

The robustness of the proposed MPC method is verified by changing certain parameters of the RPS and SPS systems. The active power-shortage scenario in Subsection B is applied as a case study. When a large power disturbance occurs, the time constants of the hydro/thermal governors ($T_{\text{Gs}i}$ and $T_{\text{Gr}k}$, respectively), the time constants of the steam turbine and reheater (T_{Tk} and $T_{\text{Rr}k}$, respectively), and the control coefficients of the EAL (K_{i} and K_{p}) either change or remain unchanged, depending on the case, as shown in Table IV. For comparison, Strategy D in Subsection B (where the proposed MPC method and EAL regulations are applied) is adopted to verify the robustness analysis.

As illustrated in Fig. 12, compared with the results for Case A, when the parameters are changed, the maximum deviation of the frequency nadir in the three cases is approximately 0.1 Hz. The injection power of VSC1

in the SPS system and the active power of the EAL vary within 30 MW and 50 MW, respectively. The results indicate that changing the parameters slightly affects the control effect, but becomes negligible after the MPC-based controllers regulating the control output. Thus, the proposed MPC method is verified to be robust to variations in the system parameters.

TABLE IV
PARAMETER CONDITION BASED ON CASE

Case	Parameter condition
A	Unchanged
B	Increased by 25%
C	Decreased by 25%

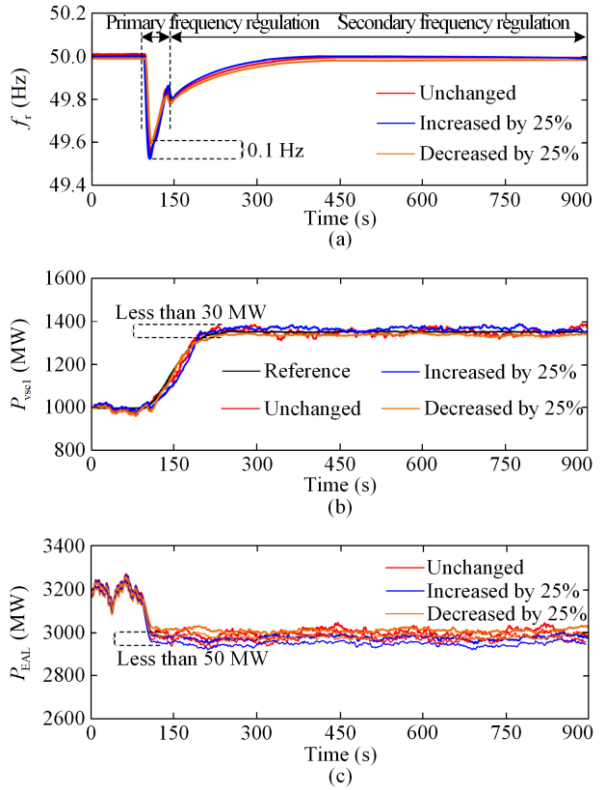

Fig. 12. Control effects of different cases for changing parameters. (a) Frequency in RPS system f_r. (b) Injection power of VSC1 in SPS system P_{vsc1}. (c) Active power consumption of EALs in SPS system P_{EAL}.

D. Efficiency Analysis

To further analyze the computational efficiency, four widely used indices are applied to measure the control performance of the proposed MPC and PI methods: the integral of the square error I_{SE}, the integral of the timed square error I_{TSE}, the integral of the absolute error I_{AE}, and the integral of the timed absolute error I_{TAE}, expressed as:

$$I_{SE} = \int_0^{t_s} (\Delta f)^2 + (\Delta P_{sps})^2 \, dt \tag{25}$$

$$I_{TSE} = \int_0^{t_s} t\left[(\Delta f)^2 + (\Delta P_{sps})^2\right] dt \tag{26}$$

$$I_{AE} = \int_0^{t_s} \left(|\Delta f| + |\Delta P_{sps}|\right) dt \tag{27}$$

$$I_{TAE} = \int_0^{t_s} t\left(|\Delta f| + |\Delta P_{sps}|\right) dt \tag{28}$$

where t_s is the sampling duration.

The small and large active power disturbance scenarios (Strategies B and D) presented in Subsections A and B are selected to analyze the control performance of the different control methods, with the performance indices listed in Table V.

TABLE V
COMPARATIVE RESULTS OF PERFORMANCE INDICES

Scenarios		Methods	Performance Indices			
			I_{SE}	I_{TSE}	I_{AE}	I_{TAE}
Small power disturbance		PI	0.68	8.96	12.78	131.66
		MPC	**0.043**	**0.081**	**0.93**	**3.89**
Large power disturbance	Shortage	PI	2.43	19.65	43.62	680.82
		MPC	**0.13**	**2.83**	**6.64**	**21.29**
	Surplus	PI	0.96	15.76	35.69	430.26
		MPC	**0.093**	**1.84**	**5.73**	**17.56**

Based on the results, in the small and large active power disturbance scenarios, the values of the performance indices of the proposed MPC method are much lower than those of the PI method, thus further verifying the rapid response regulation and improved robustness of the proposed MPC control strategy.

VI. CONCLUSION

Considering the load characteristics of electrolytic aluminum, this study proposes an active power support control strategy for a VSC-HVDC asynchronous power system. Based on an analysis of the control model of an EAL, the power consumption of the EAL can be regulated from 0.89 p.u. to 1.06 p.u. in seconds, which signifies significant regulation potential for active power support control. An LFC model of the sending and receiving sides of an asynchronous power system is demonstrated. Based on the MPC method, an active power support control strategy is deduced to maintain the frequency stability in the RPS system and transmit a steady output power from the SPS system when a large power disturbance occurs. The proposed strategy is tested using a combination of an actual industrial power system and a modified IEEE 39-bus system. The simulation results indicate that the proposed control strategy can realize steady active power support in an asynchronous power system. Compared with the PI control method, the MPC-based controllers perform better in eliminating frequency deviations in the RPS system under both small and large power disturbances. Owing to the rapid regulation of the EALs, the MPC-based controller in the SPS system demonstrates better control effects in smoothing wind power fluctuations, thus providing more stable reserve capacity support for the VSC-HVDC system. The effectiveness of

the proposed active power support control strategy is verified and its potential for further practical applications is demonstrated.

APPENDIX A

Based on the analysis in Section II, the active power consumption of the EAL can be controlled by regulating the voltage drop on the saturable reactors ΔU_{SR}. To verify the performance of the proposed control model on the EAL, an actual 330 MW EAL, as presented in [28], is selected as a case study. The load model of the EAL is constructed on an RTDS platform based on Fig. 1, with the parameters listed in Table AI.

Based on the active power control model in Fig. 2, the active power of EAL P_{EAL}, can be regulated by changing the control input ΔP_{EALref}. The regulation range of ΔU_{SR} in this case is 20–70 V. To investigate the active power regulation limits of the EAL, tests are conducted based on Table AII, and the simulation results are shown in Figs. A1 and A2.

TABLE AI
PARAMETERS OF 330 MW EAL

Parameter	Initial value
AC bus voltage U_{AC} (kV)	10.5
Voltage drop on saturable reactor U_{SR} (V)	35
DC bus voltage U_{DC} (V)	1012
Direct current in electrolyzer I_{DC} (kA)	326.1
Back electromotive force E (V)	354.6
Equivalent resistance R (mΩ)	2.016
PI controller coefficients	$K_p=10.5$, $K_i=1.5$
Time constant of electrolyzer T_{ES} (s)	2.0
Time constant of saturable reactor T_{SR} (s)	0.5
Coefficient on saturable reactor K_{SR}	7.5

TABLE AII
ACTIVE POWER REGULATION TESTS ON 330 MW EAL

Tests	Scenario
Down-regulation	5%
	10%
	15%
Up-regulation	5%
	10%

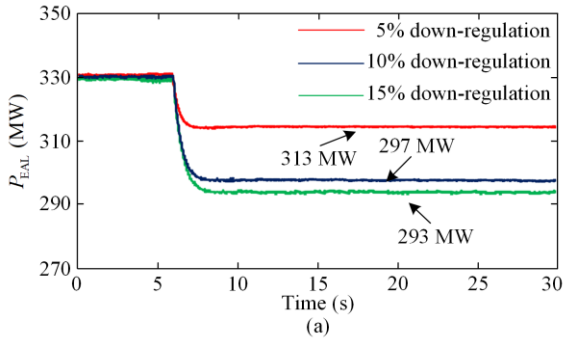

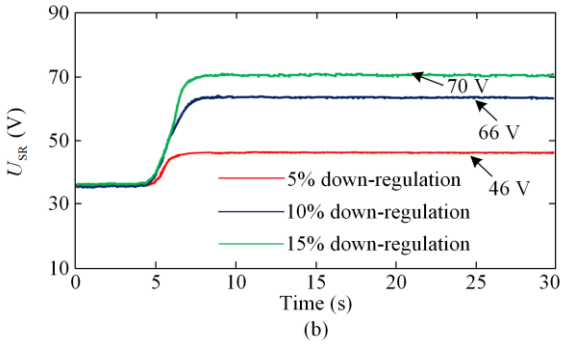

Fig. A1. Simulation results of active power down-regulation test. (a) Active power consumption of EAL P_{EAL}. (b) Voltage drop on saturable reactor U_{SR}.

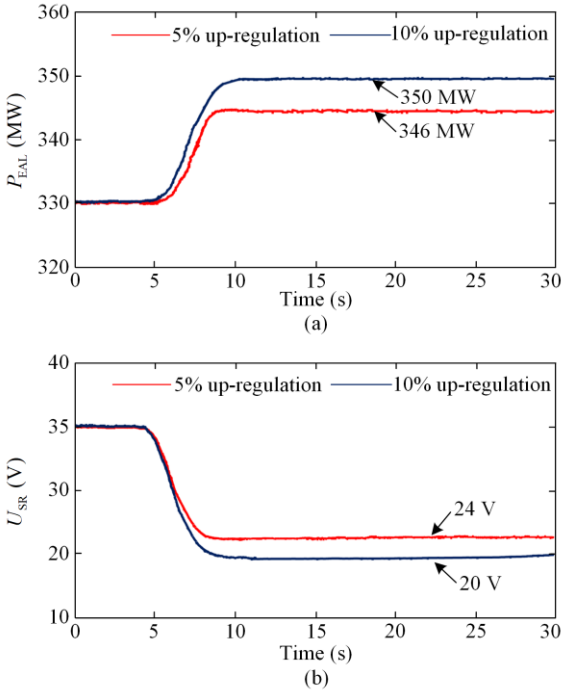

Fig. A2. Simulation results of active power up-regulation test. (a) Active power consumption of EAL P_{EAL}. (b) Voltage drop on saturable reactor U_{SR}.

Figures A1 and A2 show the results of active power P_{EAL} and the voltage drop of the saturable reactor U_{SR} when down-regulation and up-regulation are applied, respectively. When the 5%, 10%, and 15% down-regulations are applied at $t=5$ s, the voltage drops on the saturable reactor U_{SR} increase, and the active power of the EAL, P_{EAL}, is decreased within seconds. When a 15% down-regulation is applied, P_{EAL} decreases to 293 MW, whereas U_{SR} increases to the upper limit of 70 V. This implies that the maximum P_{EAL} down-regulation is 0.89 p.u., or 11%. Similarly, the active power consumption of the EAL can be up-regulated to 1.06 p.u. (350 MW) when 10%

up-regulation is applied, whereas U_{SR} decreases to its lower limit of 20 V.

In summary, the active power regulation range of the EAL in this case is 0.89–1.06 p.u., which is similar to the theoretical value calculated using (7). The simulation results indicate the effectiveness of the proposed control model for the EAL.

APPENDIX B

Based on Fig. 4, the LFC model of an SPS power system can be expressed as follows:

$$\begin{cases} \Delta\dot{f}_{\mathrm{s}} = -\dfrac{D_{\mathrm{s}}}{M_{\mathrm{s}}}\Delta f_{\mathrm{s}} + \dfrac{1}{M_{\mathrm{s}}}\Delta P_{\mathrm{G}si} - \dfrac{1}{M_{\mathrm{s}}}\Delta P_{\mathrm{EAL}j} + \dfrac{1}{M_{\mathrm{s}}}(\Delta P_{\mathrm{w}} - \Delta P_{\mathrm{vsc1}}) \\ \Delta\dot{P}_{\mathrm{G}si} = -\dfrac{2}{R_{si}T_{\mathrm{G}si}}\Delta f_{\mathrm{s}} - \Delta P_{\mathrm{G}si} + \dfrac{T_{\mathrm{G}si}+T_{\mathrm{ws}i}}{T_{\mathrm{G}si}}\Delta\mu_{si} - \dfrac{1}{T_{\mathrm{G}si}}\Delta P_{\mathrm{Gs\text{-}ref}i} \\ \Delta\dot{\mu}_{si} = -\dfrac{1}{R_{si}T_{\mathrm{G}si}}\Delta f_{\mathrm{s}} - \dfrac{1}{T_{\mathrm{G}si}}\Delta\mu_{si} + \dfrac{1}{T_{\mathrm{G}si}}\Delta P_{\mathrm{Gs\text{-}ref}i} \\ \Delta\dot{I}_{\mathrm{DC}j} = -\dfrac{1}{T_{\mathrm{ES}j}}\Delta I_{\mathrm{DC}j} + \dfrac{1}{T_{\mathrm{ES}j}K_{\mathrm{P\text{-}I}j}}\Delta P_{\mathrm{EALref}j} \\ \Delta\dot{I}_{\mathrm{DCcon}j} = \left(K_{\mathrm{I}j} - \dfrac{K_{\mathrm{P}j}}{T_{\mathrm{ES}j}}\right)\Delta I_{\mathrm{DC}j} + \dfrac{K_{\mathrm{P}j}}{T_{\mathrm{ES}j}K_{\mathrm{P\text{-}I}j}}\Delta P_{\mathrm{EALref}j} \\ \Delta\dot{P}_{\mathrm{EAL}j} = \dfrac{K_{\mathrm{P\text{-}U}j}K_{\mathrm{SR}j}}{T_{\mathrm{SR}j}}\Delta I_{\mathrm{DCcon}j} - \dfrac{1}{T_{\mathrm{SR}j}}\Delta P_{\mathrm{EAL}j} \end{cases} \tag{B1}$$

Meanwhile, the ACE signal e_{s} is expressed as:

$$e_{\mathrm{s}} = \Delta P_{\mathrm{sps}} = \left(\sum_{i=1}^{m}\Delta P_{\mathrm{G}si} - \sum_{j=1}^{n}\Delta P_{\mathrm{EAL}j} + \Delta P_{\mathrm{w}}\right) - \Delta P_{\mathrm{vsc1}} \tag{B2}$$

Combining (B1) and (B2), the LFC model of the SPS system can be described by state-space equations in (15), with matrices $\boldsymbol{A}_{\mathrm{s}}$, $\boldsymbol{B}_{\mathrm{s}}$, $\boldsymbol{C}_{\mathrm{s}}$, $\boldsymbol{P}_{\mathrm{s}}$, and $\boldsymbol{H}_{\mathrm{s}}$ expressed as follows:

$$\begin{cases} \boldsymbol{A}_{\mathrm{s}} = \begin{bmatrix} -\dfrac{D_{\mathrm{s}}}{M_{\mathrm{s}}} & \boldsymbol{A}_{12} & \boldsymbol{A}_{13} \\ \boldsymbol{A}_{21} & \boldsymbol{A}_{\mathrm{G}si} & \boldsymbol{0} \\ \boldsymbol{0} & \boldsymbol{0} & \boldsymbol{A}_{\mathrm{EAL}j} \end{bmatrix} \in \boldsymbol{R}^{(1+2i+3j)\times(1+2i+3j)} \\ \boldsymbol{B}_{\mathrm{s}} = \begin{bmatrix} \boldsymbol{0} & \boldsymbol{0} \\ \boldsymbol{B}_{\mathrm{G}si} & \boldsymbol{0} \\ \boldsymbol{0} & \boldsymbol{B}_{\mathrm{EAL}j} \end{bmatrix} \in \boldsymbol{R}^{(1+2i+3j)\times(i+j)} \\ \boldsymbol{C}_{\mathrm{s}} = \left[0, \boldsymbol{C}_{12}, \boldsymbol{C}_{13}\right] \in \boldsymbol{R}^{1\times(1+2i+3j)} \\ \boldsymbol{P}_{\mathrm{s}} = \left[-\dfrac{1}{M_{\mathrm{s}}}, \boldsymbol{0}, \boldsymbol{0}\right]^{\mathrm{T}} \in \boldsymbol{R}^{(1+2i+3j)\times 1} \\ \boldsymbol{H}_{\mathrm{s}} = 1 \end{cases} \tag{B3}$$

where the submatrices in $\boldsymbol{A}_{\mathrm{s}}$, $\boldsymbol{B}_{\mathrm{s}}$, and $\boldsymbol{C}_{\mathrm{s}}$ are expressed as:

$$\begin{cases} \boldsymbol{A}_{12} = \left[\dfrac{1}{\boldsymbol{M}_{\mathrm{s}}} \quad \boldsymbol{0}\right] \in \boldsymbol{R}^{1\times 2i} \\ \boldsymbol{A}_{13} = \left[\boldsymbol{0} \quad \boldsymbol{0} \quad -\dfrac{1}{\boldsymbol{M}_{\mathrm{s}}}\right] \in \boldsymbol{R}^{1\times 3j} \\ \boldsymbol{A}_{21} = \left[\dfrac{2}{\boldsymbol{R}_{si}\boldsymbol{T}_{\mathrm{G}si}} \quad \dfrac{-1}{\boldsymbol{R}_{si}\boldsymbol{T}_{\mathrm{G}si}}\right]^{\mathrm{T}} \in \boldsymbol{R}^{2i\times 1} \\ \boldsymbol{A}_{\mathrm{G}si} = \begin{bmatrix} -\boldsymbol{1} & \dfrac{\boldsymbol{T}_{\mathrm{G}si}+\boldsymbol{T}_{\mathrm{ws}i}}{\boldsymbol{T}_{\mathrm{G}si}} \\ \boldsymbol{0} & -\dfrac{1}{\boldsymbol{T}_{\mathrm{G}si}} \end{bmatrix} \in \boldsymbol{R}^{2i\times 2i} \\ \boldsymbol{B}_{\mathrm{G}si} = \left[-\dfrac{1}{\boldsymbol{T}_{\mathrm{G}si}} \quad \dfrac{1}{\boldsymbol{T}_{\mathrm{G}si}}\right]^{\mathrm{T}} \in \boldsymbol{R}^{2i\times 1} \\ \boldsymbol{C}_{12} = \left[\boldsymbol{1} \quad \boldsymbol{0}\right] \in \boldsymbol{R}^{1\times 2i} \\ \boldsymbol{C}_{13} = \left[\boldsymbol{0} \quad \boldsymbol{0} \quad \boldsymbol{1}\right] \in \boldsymbol{R}^{1\times 3j} \end{cases} \tag{B4}$$

The expressions for submatrices $\boldsymbol{A}_{\mathrm{EAL}j}$ and $\boldsymbol{B}_{\mathrm{EAL}j}$ have been introduced in Section II.

Similarly, the differential equations of the LFC model in the RPS power system can be deduced as follows:

$$\begin{cases} \Delta\dot{f}_{\mathrm{r}} = -\dfrac{D_{\mathrm{r}}}{M_{\mathrm{r}}}\Delta f_{\mathrm{r}} + \dfrac{1}{M_{\mathrm{r}}}\Delta P_{\mathrm{G2}k} + \dfrac{1}{M_{\mathrm{r}}}\Delta P_{\mathrm{vsc2}} - \dfrac{1}{M_{\mathrm{r}}}\Delta P_{\mathrm{D}} \\ \Delta\dot{P}_{\mathrm{G2}k} = -\dfrac{1}{T_{\mathrm{R}rk}}\Delta P_{\mathrm{G}rk} + \left(\dfrac{1}{T_{\mathrm{R}rk}} - \dfrac{K_{\mathrm{R}rk}}{T_{\mathrm{T}k}}\right)\Delta P_{\mathrm{R}rk} + \dfrac{K_{\mathrm{R}rk}}{T_{\mathrm{T}k}}\Delta X_{\mathrm{G}rk} \\ \Delta\dot{P}_{\mathrm{R}rk} = -\dfrac{1}{T_{\mathrm{T}k}}\Delta P_{\mathrm{R}rk} + \dfrac{1}{T_{\mathrm{T}k}}\Delta X_{\mathrm{G}rk} \\ \Delta\dot{X}_{\mathrm{G}rk} = -\dfrac{1}{T_{\mathrm{G}rk}R_{rk}}\Delta f_{\mathrm{r}} - \dfrac{1}{T_{\mathrm{G}rk}}\Delta X_{\mathrm{G}rk} + \dfrac{1}{T_{\mathrm{G}rk}}\Delta P_{\mathrm{Gr\text{-}ref}k} \end{cases} \tag{B5}$$

Subsequently, the LFC model in the RPS system can be expressed by state-space equations in (16). The matrices $\boldsymbol{A}_{\mathrm{r}}$, $\boldsymbol{B}_{\mathrm{r}}$, $\boldsymbol{C}_{\mathrm{r}}$, and $\boldsymbol{P}_{\mathrm{r}}$ are expressed as follows:

$$\begin{cases} \boldsymbol{A}_{\mathrm{r}} = \begin{bmatrix} -\dfrac{D_{\mathrm{r}}}{M_{\mathrm{r}}} & \dfrac{\boldsymbol{1}}{\boldsymbol{M}_{\mathrm{r}}} & \boldsymbol{0} & \boldsymbol{0} \\ \boldsymbol{0} & -\dfrac{1}{\boldsymbol{T}_{\mathrm{G}rk}} & \dfrac{1}{\boldsymbol{T}_{\mathrm{R}rk}} - \dfrac{\boldsymbol{K}_{\mathrm{R}rk}}{\boldsymbol{T}_{\mathrm{T}k}} & \dfrac{\boldsymbol{K}_{\mathrm{R}rk}}{\boldsymbol{T}_{\mathrm{T}k}} \\ \boldsymbol{0} & \boldsymbol{0} & -\dfrac{1}{\boldsymbol{T}_{\mathrm{T}k}} & \dfrac{1}{\boldsymbol{T}_{\mathrm{T}k}} \\ -\dfrac{1}{\boldsymbol{T}_{\mathrm{G}rk}\boldsymbol{R}_{rk}} & \boldsymbol{0} & \boldsymbol{0} & -\dfrac{1}{\boldsymbol{T}_{\mathrm{G}rk}} \end{bmatrix} \in \boldsymbol{R}^{(1+3k)\times(1+3k)} \\ \boldsymbol{B}_{\mathrm{r}} = \begin{bmatrix} \boldsymbol{0} & \boldsymbol{0} & \boldsymbol{0} & \dfrac{1}{\boldsymbol{T}_{\mathrm{G}rk}} \\ \dfrac{1}{\boldsymbol{M}_{\mathrm{r}}} & \boldsymbol{0} & \boldsymbol{0} & \boldsymbol{0} \end{bmatrix}^{\mathrm{T}} \in \boldsymbol{R}^{(1+3k)\times(1+k)} \\ \boldsymbol{C}_{\mathrm{r}} = \left[1, \boldsymbol{0}, \boldsymbol{0}, \boldsymbol{0}\right] \in \boldsymbol{R}^{1\times(1+3k)} \\ \boldsymbol{P}_{\mathrm{r}} = \left[-\dfrac{1}{M_{\mathrm{r}}}, \boldsymbol{0}, \boldsymbol{0}, \boldsymbol{0}\right]^{\mathrm{T}} \in \boldsymbol{R}^{(1+3k)\times 1} \end{cases} \tag{B6}$$

ACKNOWLEDGMENT

Not applicable.

AUTHOR'S CONTRIBUTIONS

Xin Ding: algorithms formulation and manuscript writing. Siyang Liao: simulation and manuscript revising. Jian Xu: conceptualization and methodology. Yuanzhang Sun: supervision and reviewing. All authors read and approved the final manuscript.

FUNDING

This work is supported by the Science and Technology Project of China Southern Power Grid (No. 050000202 2030301GH00163).

AVAILABILITY OF DATA AND MATERIALS

Not applicable.

DECLARATIONS

Competing interests: The authors declare that they have no known competing financial interests or personal relationships that could have appeared to influence the work reported in this article.

AUTHORS' INFORMATION

Xin Ding received the B.S. degree in electrical engineering and automation from the Shanghai University of Electrical Power, Shanghai, China, in 2014, and the Ph.D. degree in power engineering from Wuhan University, Wuhan, China, in 2022. He is now working at Shanghai University of Electric Power. His research interests include operation and analysis of power system with renewable energy and load control.

Siyang Liao received the B.S. and Ph.D. degrees in electrical engineering from Wuhan University, Wuhan, China, in 2011 and 2016, respectively. He is currently an associated professor with the School of Electrical Engineering and Automation, Wuhan University. His research interests include wind power integration and power system simulation.

Jian Xu received the B.S. and Ph.D. degrees in electrical engineering from Wuhan University, Wuhan, China, in 2002 and 2007, respectively. He is currently a professor with the School of Electrical Engineering and Automation, Wuhan University. His research interests include power system operation, voltage stability, and wind power control and integration.

Yuanzhang Sun received the B.S. degree from the Wuhan University of Hydro and Electrical Engineering, Wuhan, China, in 1987, the M.S. degree from the Electric Power Research Institute (EPRI), Beijing, China, in 1982, and the Ph.D. degree in electrical engineering from Tsinghua University, Beijing, in 1988. He is currently a professor with the School of Electrical Engineering in Wuhan University, and the chair professor with the Department of Electrical Engineering and the Vice Director of the State Key Lab of Power System Control and Simulation, Tsinghua University. His main research interests include the areas of power system dynamics and control, wind power, voltage stability and control, and reliability.

REFERENCES

[1] K. Fang, C. Li, and Y. Tang *et al.*, "China's pathways to peak carbon emissions: new insights from various industrial sectors," *Applied Energy*, vol. 306, Jan. 2022.

[2] S. Liu, B. Cai, and M. Gao *et al.*, "Empirical evidence for the edge of a centralized regional market over a cross-province balancing market in allocating electricity resources: a case study of Yunnan in China," *Energy Reports*, vol. 9, pp. 911-921, Sept. 2023.

[3] B. Zhou, H. Rao, and W. Wu *et al*., "Principle and application of asynchronous operation of China Southern Power Grid," *IEEE Journal of Emerging and Selected Topics in Power Electronics*, vol. 6, no. 3, pp. 1032-1040, Sept. 2018.

[4] K. Sun, H. Xiao, and L. Sundaresh *et al*., "Frequency response reserves sharing across asynchronous grids through MTDC system," *IET Generation, Transmission & Distribution*, vol. 13, no. 21, pp. 4952-4959, Nov. 2019.

[5] Z. Li, Z. Wei, and R. Zhan *et al*., "Frequency support control method for interconnected power systems using VSC-MTDC," *IEEE Transactions on Power Systems*, vol. 36, no. 3, pp. 2304-2313, May 2021.

[6] K. Jose, T. Joseph, and J. Liang *et al*., "Auxiliary dead-band controller for the coordination of fast frequency support from multi-terminal HVDC grids and offshore wind farms," *IET Renewable Power Generation*, vol. 12, no. 13, pp. 1444-1452, Sept. 2018.

[7] O. Adeuyi, M. Cheah-Mane, and J. Liang *et al*., "Fast frequency response from offshore multiterminal VSC-HVDC schemes," *IEEE Transactions on Power Delivery*, vol. 32, no. 6, pp. 2442-2452, Dec. 2017.

[8] A. Junyent-Ferr, Y. Pipelzadeh, and T. Green, "Blending HVDC-link energy storage and offshore wind turbine inertia for fast frequency response," *IEEE Transactions on Sustainable Energy*, vol. 6, no. 3, pp. 1059-1066, Jul. 2015.

[9] Y. Cao, W. Wang, and Y. Li *et al*., "A virtual synchronous generator control strategy for VSC-MTDC systems," *IEEE Transactions on Energy Conversion*, vol. 33, no. 2, pp. 750-761, Jun. 2018.

[10] K. Qu, D. Guo, and C. Pan *et al.*, "Model predictive dual-loop cooperative optimal control strategy based on an optical storage virtual synchronous generator" *Power System Protection and Control*, vol. 52, no. 18, pp. 149-157, Sept. 2024. (in Chinese)

[11] M. A. Abdelwahed and E. F. El-Saadany, "Power sharing control strategy of multiterminal VSC-HVDC transmission systems utilizing adaptive voltage droop,"

IEEE Transactions on Sustainable Energy, vol. 8, no. 2, pp. 605-615, Apr. 2017.

[12] K. Rouzbehi, A. Miranian, and J. I. Candela *et al*., "A generalized voltage droop strategy for control of multiterminal DC grids," *IEEE Transactions on Industry Applications*, vol. 51, no. 1, pp. 607-618, Feb. 2015.

[13] H. Rao, W, Wu, and T. Mao *et al*., "Frequency control at the power sending side for HVDC asynchronous interconnections between Yunnan power grid and the rest of CSG," *CSEE Journal of Power and Energy Systems*, vol. 7, no. 1, pp. 105-113, Jan. 2021.

[14] M. Hassan, R. Shah, and J. Hossain, "Frequency regulation of multiple asynchronous grids using adaptive droop in high-voltage direct current system," *IET Generation, Transmission & Distribution*, vol. 14, no. 7, pp. 1389-1399, Feb. 2020.

[15] Q. Zhang, J. D. McCalley, and V. Ajjarapu *et al*., "Primary frequency support through North American continental HVDC interconnections with VSC-MTDC systems," *IEEE Transactions on Power Systems*, vol. 36, no. 1, pp. 806-817, Aug. 2020.

[16] J. E. S. de Haan, C. E. Concha, and M. Gibescu *et al.*, "Stabilising system frequency using HVDC between the Continental European, Nordic, and Great Britain systems," *Sustainable Energy, Grids and Networks*, vol. 5, pp. 125-134, Mar. 2016.

[17] S. Liao, J. Xu, and Y. Sun *et al*., "Control of energy-intensive load for power smoothing in wind power plants," *IEEE Transactions on Power Systems*, vol. 33, no.6, pp. 6142-6154, Nov. 2018.

[18] Y. Bao, J. Xu, and S. Liao *et al*., "Field verification of frequency control by energy-intensive loads for isolated power systems with high penetration of wind power," *IEEE Transactions on Power Systems*, vol. 33, no. 6, pp. 6098-6108, Nov. 2018.

[19] C. Zhang, W. Lin, and D. Ke *et al*., "Smoothing tie-line power fluctuations for industrial microgrids by demand side control: an output regulation approach," *IEEE Transactions on Power Systems*, vol. 34, no. 5, pp. 3716-3728, Sept. 2019.

[20] X. Ding, J. Xu, and Y. Sun *et al*., "A demand side controller of electrolytic aluminum industrial microgrids considering wind power fluctuations," *Protection and Control of Modern Power Systems*, vol. 7, no. 4, pp. 1-13, Dec. 2022.

[21] N. Zhao, S. Gorbachev, and D. Yue *et al*., "Model predictive based frequency control of power system in corporating air-conditioning loads with communication delay," *International Journal of Electrical Power & Energy Systems*, vol. 138, Jan. 2022.

[22] S. Gorbachev, J. Guo, and A. Mani *et al*., "MPC-based LFC for interconnected power systems with PVA and ESS under model uncertainty and communication delay," *Protection and Control of Modern Power Systems*, vol. 8, no. 4, pp. 1-17, Oct. 2023.

[23] M. M. Gulzar, "Designing of robust frequency stabilization using optimized MPC-(1+PIDN) controller for high order interconnected renewable energy based power systems," *Protection and Control of Modern Power Systems*, vol. 8, no. 1, pp. 1-14, Jan. 2023.

[24] P. McNamara and F. Milano, "Model predictive control-based AGC for multi-terminal HVDC-connected ac grids," *IEEE Transactions on Power Systems*, vol. 33, no. 1, pp. 1036-1048, Jan. 2018.

[25] L. Papangelis, M.-S. Debry, and P. Panciatici *et al*., "A receding horizon approach to incorporate frequency support into the AC/DC converters of a multi-terminal DC grid," *Electric Power Systems Research*, vol. 148, pp. 1-9, Apr. 2017.

[26] L. Papangelis, M. S. Debry, and T. Prevost *et al*., "Decentralized model predictive control of voltage source converters for AC frequency containment," *International Journal of Electrical Power & Energy Systems*, vol. 98, pp. 342-349, Jun. 2018.

[27] J. Xu, S. Liao, and Y. Sun *et al*., "An isolated industrial power system driven by wind-coal power for aluminum productions: a case study of frequency control," *IEEE Transactions on Power Systems*, vol. 30, no. 1, pp. 471-483, Jan. 2015.

[28] S. Liao, J. Xu, and Y. Sun *et al*., "Local utilization of wind electricity in isolated power systems by employing coordinated control scheme of industrial energy-intensive load," *Applied Energy*, vol. 217, pp. 14-24, May 2018.

[29] H. Jiang, J. Lin, and Y. Song *et al*., "Demand side frequency control scheme in an isolated wind power system for industrial aluminum smelting production," *IEEE Transactions on Power Systems*, vol. 29, no. 2, pp. 844-853, Mar. 2014.

[30] B. Appasani, A. V. Jha, and S. Kumar Mishra *et al*., "Communication infrastructure for situational awareness enhancement in WAMS with optimal PMU placement," *Protection and Control of Modern Power Systems*, vol. 6, no. 1, pp. 1-12, Jan. 2021.